
STAF: Sinusoidal Trainable Activation Functions for Implicit Neural Representation

Alireza Morsali¹ MohammadJavad Vaez² Hossein Soltani³ Amirhossein Kazerouni^{4 5 6} Babak Taati^{4 5 6}
Morteza Mohammad-Noori²

Abstract

Implicit Neural Representations (INRs) have emerged as a powerful framework for modeling continuous signals. The spectral bias of ReLU-based networks is a well-established limitation, restricting their ability to capture fine-grained details in target signals. While previous works have attempted to mitigate this issue through frequency-based encodings or architectural modifications, these approaches often introduce additional complexity and do not fully address the underlying challenge of learning high-frequency components efficiently. We introduce **Sinusoidal Trainable Activation Functions (STAF)**, designed to directly tackle this limitation by enabling networks to adaptively learn and represent complex signals with higher precision and efficiency. STAF inherently modulates its frequency components, allowing for self-adaptive spectral learning. This capability significantly improves convergence speed and expressivity, making STAF highly effective for both signal representations and inverse problems. Through extensive evaluations, we demonstrate that STAF outperforms state-of-the-art (SOTA) methods in accuracy and reconstruction fidelity with superior Peak Signal-to-Noise Ratio (PSNR). These results establish STAF as a robust solution for overcoming spectral bias and the capacity-convergence gap, making it valuable for computer graphics and related fields. Our codebase is publicly accessible on the <https://github.com/AlirezaMorsali/STAF>.

¹Department of Electrical Engineering, McGill University, Canada ²School of Mathematics, Statistics, and Computer Science, University of Tehran, Iran ³Independent Researcher ⁴Department of Computer Science, University of Toronto, Canada ⁵Vector Institute, Canada ⁶KITE Research Institute, University Health Network, Canada. Correspondence to: Alireza Morsali <alireza.morsali@mail.mcgill.ca>, MohammadJavad Vaez <mjvaez@ut.ac.ir>, Hossein Soltani <mohammad.hossein19soltani@gmail.com>, Amirhossein Kazerouni <amirhossein@cs.toronto.edu>, Babak Taati <babak.taati@uhn.ca>, Morteza Mohammad-Noori <mm-noori@ut.ac.ir>.

1. Introduction

INRs have transformed signal processing and computer vision by shifting from discrete grid-based methods to continuous data mapping using neural networks, particularly Multilayer Perceptrons (MLPs). This approach enables the processing of diverse data types and complex relationships, driving advancements in computer graphics and computational photography (Mildenhall et al., 2020; Sitzmann et al., 2020; Tancik et al., 2020). INRs have been instrumental in novel view synthesis, 3D reconstruction, and tackling high-dimensional data challenges, such as rendering complex shapes and modeling light interactions (Mildenhall et al., 2020; Sitzmann et al., 2020; Chen et al., 2021; Mescheder et al., 2019; Saragadam et al., 2022). Despite their versatility, traditional INR architectures—particularly ReLU-based networks—face limitations due to spectral bias, which hinders the reconstruction of fine details (Rahaman et al., 2019).

To address these challenges, we propose the **Sinusoidal Trainable Activation Function (STAF)**, a novel family of parametric, trainable activation functions that enhance the expressive power and performance of INRs in modeling complex signals. STAF generalizes periodic activation functions like SIREN (Sitzmann et al., 2020), which uses a single sinusoidal term with fixed phase and frequency, by introducing trainable parameters for greater flexibility. This development addresses challenges identified in earlier works regarding training networks with periodic activations (Lapedes & Farber, 1987; Parascandolo et al., 2016; Mehta et al., 2021) and expands the application of Fourier series in INRs (Gallant & White, 1988; Tancik et al., 2020; Shivapriya et al., 2021; Liao, 2020). Our findings indicate that STAF improves neural network performance in high-fidelity applications like computer graphics and data compression. Our work makes the following key **contributions**:

- **Novel Initialization Scheme:** We propose a mathematically rigorous initialization scheme that introduces a unique probability density function for initialization, providing a more robust foundation for training compared to methods relying on the central limit theorem and specific conditions, such as SIREN.
- **Expressive Power:** STAF significantly expands the set of potential frequencies compared to SIREN. Leveraging

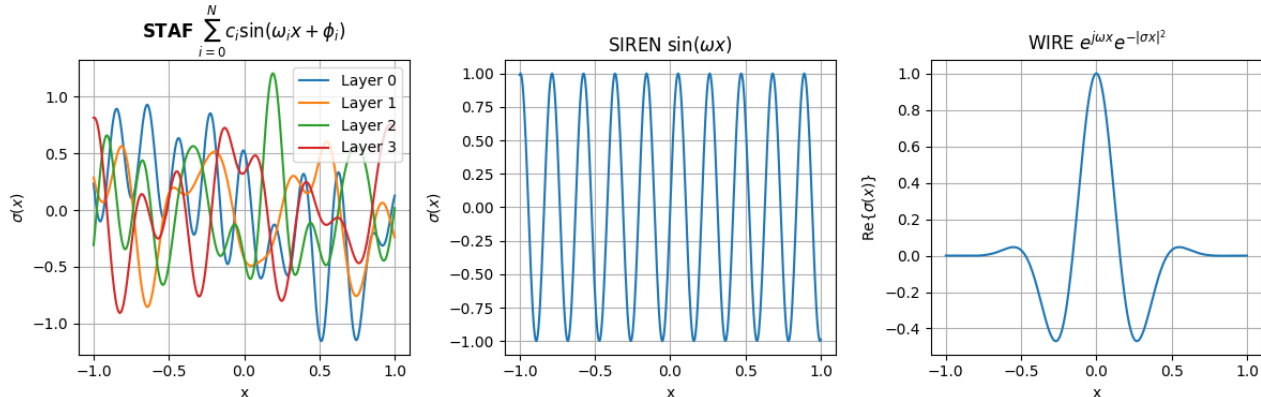


Figure 1. Activation functions used in INRs plotted over the range $[-1, 1]$. STAF utilizes a parameterized Fourier series activation, offering flexible frequency-domain adaptation. SIREN employs a sinusoidal function, providing a periodic activation landscape. WIRE employs a complex Gabor wavelet activation, balancing spatial and frequency localization.

a general theorem rooted in the Kronecker product, we provide **Theorems 5.5** and **5.7**, which introduce novel theoretical insights applicable to a broad class of trainable activation functions. These contributions are underpinned by combinatorial and algebraic tools, offering a framework that generalizes beyond the scope of STAF.

- **NTK Eigenvalues and Eigenfunctions:** We analyze the Neural Tangent Kernel (NTK) of our network, showing that its eigenvalues and eigenfunctions provide improved criteria for the learning process and convergence, enhancing understanding and performance during training.
- **Performance Improvements:** Our proposed activation function achieves significant PSNR gains across a range of signal representation tasks, including image, shape, and audio representation, as well as inverse problems such as image super-resolution and denoising. These advancements stem from faster convergence and enhanced accuracy, establishing STAF as a superior alternative to state-of-the-art models, including INCODE (Kazerouni et al., 2024), FINER (Liu et al., 2024b), WIRE (Saragadam et al., 2023), SIREN (Sitzmann et al., 2020), KAN (Liu et al., 2024a), Gaussian (Ramasinghe & Lucey, 2022), and FFN (Tancik et al., 2020).

2. Related Works

INRs have advanced in representing various signals, including images and 3D scenes, with applications in SDFs, audio signals, and data compression. Sitzmann et al.’s sine-based activations in INRs (Sitzmann et al., 2020) improved fidelity but faced slow training. Dual-MLP architectures (Mehta et al., 2021), input division into grids (Aftab et al., 2022; Kadarvish et al., 2021), and adaptive resource allocation (Martel et al., 2021; Saragadam et al., 2022) further enhanced INR capabilities. Mildenhall et al.’s volume ren-

dering for 3D scene representation in NeRF (Mildenhall et al., 2020) inspired subsequent enhancements (Chen et al., 2024; Barron et al., 2023; Kazerouni et al., 2024; Xu et al., 2023; Lin et al., 2024; Li et al., 2025; Uy et al., 2024; Reiser et al., 2021) for improved fidelity and expedited rendering.

The development of neural networks has been significantly influenced by advancements in activation functions. Early non-periodic functions like Sigmoid suffered from vanishing gradient issues in deep networks, which were later addressed by unbounded functions such as ReLU (Nair & Hinton, 2010) and its variants (Maas et al., 2013; Elfwing et al., 2018; Hendrycks & Gimpel, 2016). Adaptive functions like SinLU (Paul et al., 2022), TanhSoft (Biswas et al., 2021), and Swish (Ramachandran et al., 2017) introduced trainable parameters to better adapt to data non-linearity. However, the spectral bias in ReLU-based networks, as highlighted by Rahaman et al. (Rahaman et al., 2019), led to a preference for low-frequency signals, limiting their ability to capture fine details. To address this, periodic activation functions emerged as promising solutions for INRs, enabling the learning of high-frequency details. Early challenges in training networks with periodic activations (Lapedes & Farber, 1987; Parascandolo et al., 2016) were eventually overcome, leading to successful applications in complex data representation (Sitzmann et al., 2020; Mehta et al., 2021). Fourier Neural Networks (Gallant & White, 1988) and the Fourier feature mapping (Tancik et al., 2020) further advanced the integration of the Fourier series into neural networks. Recently, the Kolmogorov-Arnold Network (KAN) (Liu et al., 2024a; SS et al., 2024) has emerged as a promising architecture in the realm of INRs. KAN leverages Kolmogorov-Arnold representation frameworks to improve the modeling and reconstruction of complex signals, demonstrating notable performance in various INR tasks. However, as we will demonstrate in our experimental results, STAF outperforms

KAN in terms of accuracy, convergence speed, and PSNR. This paper introduces STAF, a parametric periodic activation function for MLP-based INRs, designed to enhance convergence and capture fine details with superior fidelity in high-frequency signal representation.

3. STAF: Sinusoidal Trainable Activation Function

3.1. INR Problem Formulation

INRs employ MLPs as a method for representing continuous data. At the core of INR is the function $f_{\theta} : \mathbb{R}^{F_0} \rightarrow \mathbb{R}^{F_L}$, where F_0 and F_L represent the dimensions of the input and output spaces, respectively, and θ denotes the parameters of the MLP. The objective is to approximate a target function $g(\mathbf{x})$ such that $g(\mathbf{x}) \approx f_{\theta}(\mathbf{x})$. For example, in image processing, $g(\mathbf{x})$ could be a function mapping pixel coordinates to their respective values.

As mentioned in (Yüce et al., 2022), the majority of INR architectures can be decomposed into a mapping function $\gamma : \mathbb{R}^D \rightarrow \mathbb{R}^T$ followed by an MLP, with weights $\mathbf{W}^{(l)} \in \mathbb{R}^{F_l \times F_{l-1}}$ and activation function $\rho^{(l)} : \mathbb{R} \rightarrow \mathbb{R}$, applied element-wise at each layer $l = 1, \dots, L-1$. In other words, if we represent $\mathbf{z}^{(l)}$ as the post-activation output of each layer, most INR architectures compute

$$\begin{aligned} \mathbf{z}^{(0)} &= \gamma(\mathbf{r}), \\ \mathbf{z}^{(l)} &= \rho^{(l)}(\mathbf{W}^{(l)} \mathbf{z}^{(l-1)} + \mathbf{B}^{(l)}), \quad l = 1, \dots, L-1, \end{aligned} \quad (1)$$

$$f_{\theta}(\mathbf{r}) = \mathbf{W}^{(L)} \mathbf{z}^{(L-1)} + \mathbf{B}^{(L)}.$$

Additionally, corresponding to the i 'th neuron of the l 'th layer, we employ the symbols $a_i^{(l)}$ and $z_i^{(l)}$ for the pre-activation and post-activation functions respectively. The choice of the activation function ρ is pivotal in INR, as it influences the network's ability to represent signals. Traditional functions, such as ReLU, may not effectively capture high-frequency components. The novel parametric periodic activation function, i.e., STAF, enhances the network's capability to accurately model and reconstruct complex, high-frequency signals.

3.2. STAF Activation Function

The activation function STAF introduces a conceptually different approach compared to conventional activation functions (see Figure 1). It is parameterized in the form of a Fourier series:

$$\rho^*(x) = \sum_{i=1}^{\tau} C_i \sin(\Omega_i x + \Phi_i), \quad (2)$$

where C_i , Ω_i , and Φ_i represent the *amplitude*, *frequency*, and *phase* parameters, respectively. These parameters are

learned dynamically during training, enabling the network to adapt its activation function to the specific characteristics of the signal being modeled. The use of a Fourier series is motivated by its ability to represent signals efficiently, capturing essential components with a small number of coefficients. This adaptability allows STAF to provide a compact and flexible representation for complex patterns in various tasks.

3.3. STAF Training Process

During training, STAF optimizes not only the traditional MLP parameters (weights and biases), but also the coefficients of the activation function. This dual optimization approach ensures that the network learns both an optimal set of transformations (through weights and biases) and an ideal way of activating neurons (through the parametric activation function) for each specific task. The training employs a reconstruction loss function designed to minimize the difference between the target function $g(\mathbf{x})$ and the network's approximation $f_{\theta}(\mathbf{x})$, while also encouraging efficient representation inspired by Fourier series.

3.4. Implementation Strategies

The implementation of STAF's parametric activation functions can be approached in three ways:

❶ **Individual Neuron Activation:** This method assigns a unique activation function to each neuron. It offers high expressiveness but leads to a significant increase in the number of trainable parameters, making it impractical for large networks due to potential overfitting and computational inefficiencies.

❷ **Uniform Network-wide Activation:** Here, a single shared activation function is used across the entire network. This approach simplifies the model by reducing the number of additional parameters but limits the network's expressiveness and adaptability. It may struggle to capture diverse patterns and details in complex signals.

❸ **Layer-wise Shared Activation:** This balanced strategy employs a distinct shared activation function for each layer which is also used for all experiments in this paper. For example, in a 3-layer MLP with $\tau = 25$ terms, only 225 additional parameters are required. This approach optimally balances expressiveness and efficiency, allowing each layer to develop specialized activation dynamics for the features it processes. It aligns with the hierarchical nature of MLPs, where different layers capture different signal abstractions, providing an efficient learning mechanism tailored to each layer's role.

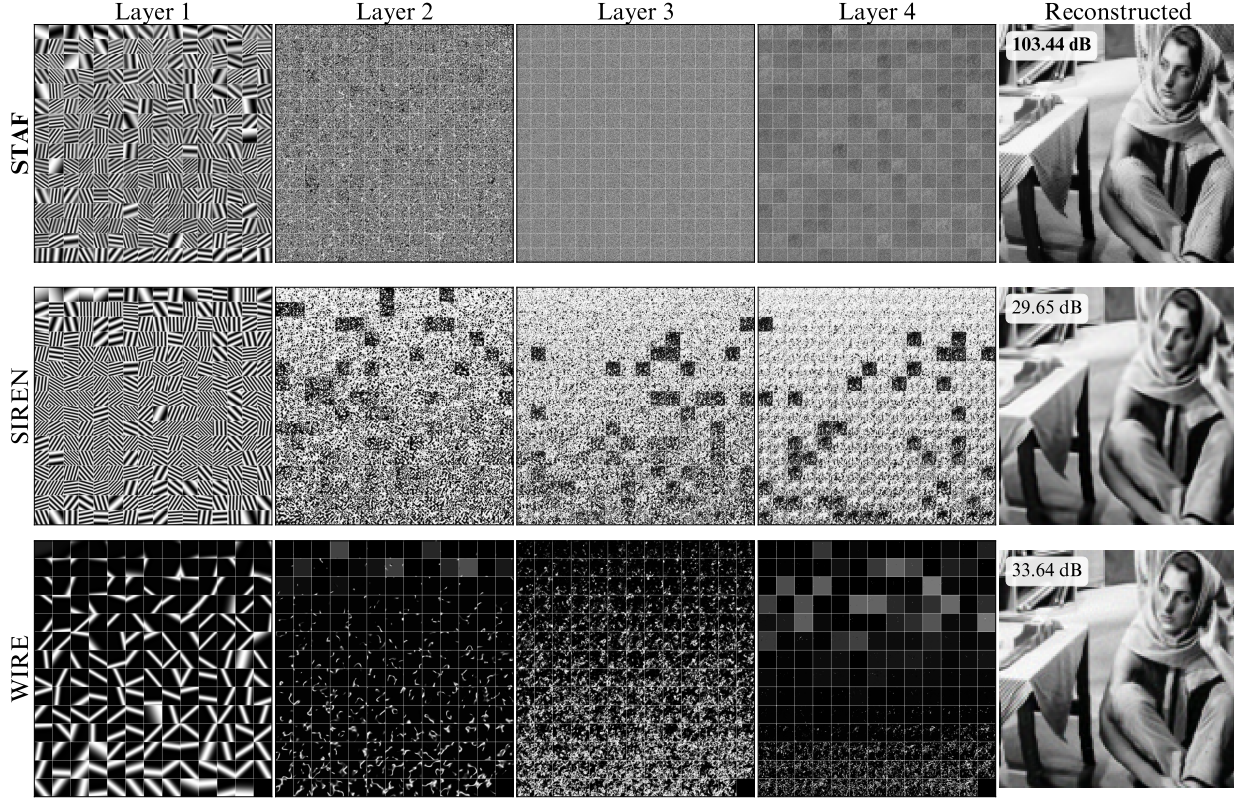


Figure 2. Activation maps for STAF, SIREN, and WIRE learned during the image reconstruction task.

3.5. Initialization

In this section, we present an initialization strategy tailored for networks utilizing STAF as the activation function. While STAF shares similarities with SIREN (Sitzmann et al., 2020), which employs \sin as its activation function, our initialization scheme is specifically designed to leverage the unique parameterization of STAF. To provide context, we first revisit the key aspects of SIREN’s initialization scheme as discussed in (Sitzmann et al., 2020), and then highlight how our approach builds upon and extends these principles to enhance network performance and stability.

In SIREN (Sitzmann et al., 2020), the input X of a single neuron follows a uniform distribution $U(-1, 1)$, and the activation function employed is $\rho(u) = \sin(u)$. Consequently, the output of the neuron is given by $Y = \sin(aX + b)$, where $a, b \in \mathbb{R}$. The authors of (Sitzmann et al., 2020) claim that regardless of the choice of b , if $a > \frac{\pi}{2}$, the output Y follows an arcsine distribution, denoted as $\text{Arcsine}(-1, 1)$. However, it becomes apparent that this claim is not correct upon further examination. If the claim were true, $\mathbb{E}[Y]$ would be independent of b . Let’s calculate it in a more general case, where instead of the interval $[-1, 1]$, we consider an arbitrary interval $[c, d]$ for the input X .

$$\begin{aligned} \mathbb{E}[Y] &= \int_c^d \sin(ax + b) f_X(x) dx \\ &= \frac{1}{d - c} \int_c^d (\sin(ax) \cos b + \sin b \cos(ax)) dx, \\ &= \frac{1}{a(d - c)} \left[(\cos(ac) - \cos(ad)) \cos b \right. \\ &\quad \left. + (\sin(ad) - \sin(ac)) \sin b \right]. \end{aligned} \quad (3)$$

Assuming $c = -1$ and $d = 1$, the result will be $\frac{2 \sin a \sin b}{a(d - c)}$, which obviously depends on a and b . However, if we want to eliminate b from $\mathbb{E}[Y]$, we can set $ad = ac + 2n\pi$, or equivalently

$$d = c + \frac{2n\pi}{a}, \quad (4)$$

for an $n \in \mathbb{N}$. Next, let us consider the next moments of Y , because if the moment-generating function (MGF) of Y exists, the moments can uniquely determine the distribution of Y .

$$\mathbb{E}[Y^k] = \int_c^d \frac{\sin^k(ax + b)}{d - c} dx \quad (5)$$

Using (4), it is equal to

$$\frac{1}{2n\pi} \int_c^{c+\frac{2n\pi}{a}} \sin^k(ax+b)dx \quad (6)$$

By assuming $u = ax + b$, we have

$$\mathbb{E}[Y^k] = \frac{1}{2an\pi} \int_{ac+b}^{ac+b+2n\pi} \sin^k(u)du. \quad (7)$$

Since for each pair of natural numbers (k, n) , $2n\pi$ is a period of $\sin^k(u)$, we can write

$$\mathbb{E}[Y^k] = \frac{1}{2an\pi} \int_0^{2\pi} \sin^k(u)du = \begin{cases} 0, & \text{if } k \text{ is odd} \\ \frac{\binom{k}{k/2}}{2^k an}, & \text{if } k \text{ is even} \end{cases} \quad (8)$$

As shown, the moments of Y (and thus the distribution of Y) depend on a (the weight multiplied by the input) and n (a parameter defining the range of input).

In the subsequent parts of (Sitzmann et al., 2020), the authors assumed that the outputs of the first layer follow a distribution of *arcsine* and fed those outputs into the second layer. By relying on the central limit theorem (CLT), they demonstrated that the output of the second layer, for each neuron, conforms to a normal distribution. Additionally, in Lemma 1.6 (Sitzmann et al., 2020), they established that if $X \sim \mathcal{N}(0, 1)$ and $Y = \sin(\frac{\pi}{2}X)$, then $Y \sim \text{Arcsine}(-1, 1)$. However, it should be noted that to prove this result, they relied on several approximations. Through induction, they asserted that the inputs of subsequent layers follow an arcsine distribution, while the outputs of these layers exhibit a normal distribution.

In contrast to the approach taken by (Sitzmann et al., 2020), the method presented in this study does not depend on the specific distributions of the input vector \mathbf{r} and weight matrices $\mathbf{W}^{(l)}$. As a result, there is no need to map the inputs to the interval $[-1, 1]$. Additionally, this method does not rely on making any approximations or the central limit theorem, which assumes large numbers. Overall, it offers a more rigorous mathematical framework. To pursue this goal, notice the following theorem.

Theorem 3.1. Consider a neural network as defined in (1) with a sinusoidal trainable activation function (STAF) defined in (2). Suppose for each i , $\Phi_i \sim U(-\pi, \pi)$. Furthermore, let C_i be i.i.d. random variables with the following probability density function:

$$f_{C_i}(c_i) = \frac{\tau|c_i|}{2} e^{-\frac{\tau c_i^2}{2}}, \quad (9)$$

and assume that C_i 's are independent of Ω_i , \mathbf{w} , \mathbf{x} , and Φ_i . Then, every post-activation will follow a $\mathcal{N}(0, 1)$ distribution (please refer to the proof in Appendix C.1.)

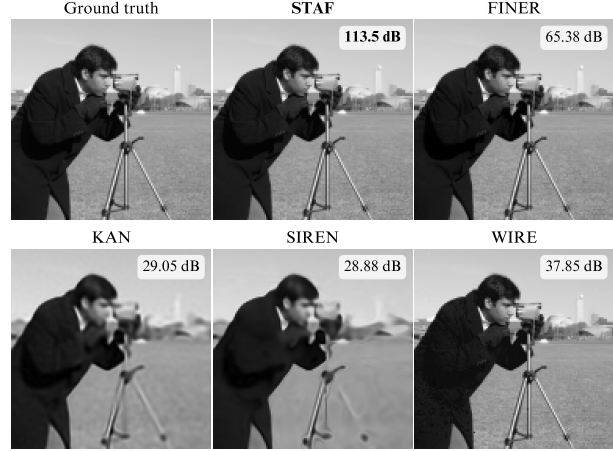


Figure 3. Ground truth image followed by reconstructions using STAF, FINER, KAN, SIREN, WIRE.

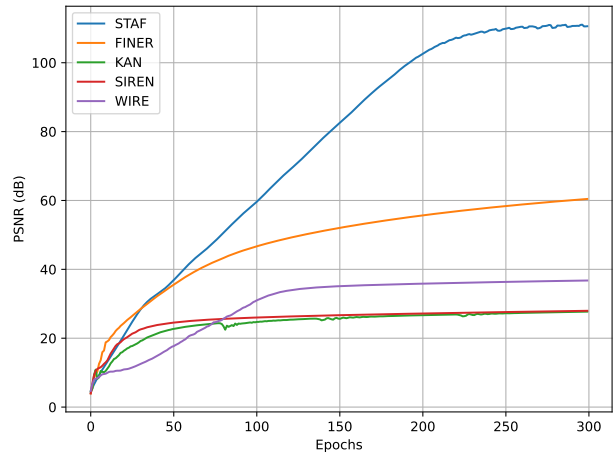


Figure 4. PSNR values achieved over 300 training iterations.

This initial setting, where every post-activation follows a standard normal distribution, is beneficial because it prevents the post-activation values from vanishing or exploding. This ensures that the signals passed from layer to layer remain within a manageable range, particularly in the first epoch. The first epoch is crucial as it establishes the foundation for subsequent learning. If the learning process is well-posed and there is sufficient data, the training process is likely to converge to a stable and accurate solution. Therefore, while it is important to monitor for potential issues in later epochs, the concern about vanishing or exploding values is significantly greater during the initial stages. Proper initialization helps mitigate these risks early on, facilitating smoother and more effective training overall.

4. Experimental Results

We evaluated SOTA models for image, audio, and shape representations, as well as inverse problems such as super-resolution and image denoising. Specifically, we used

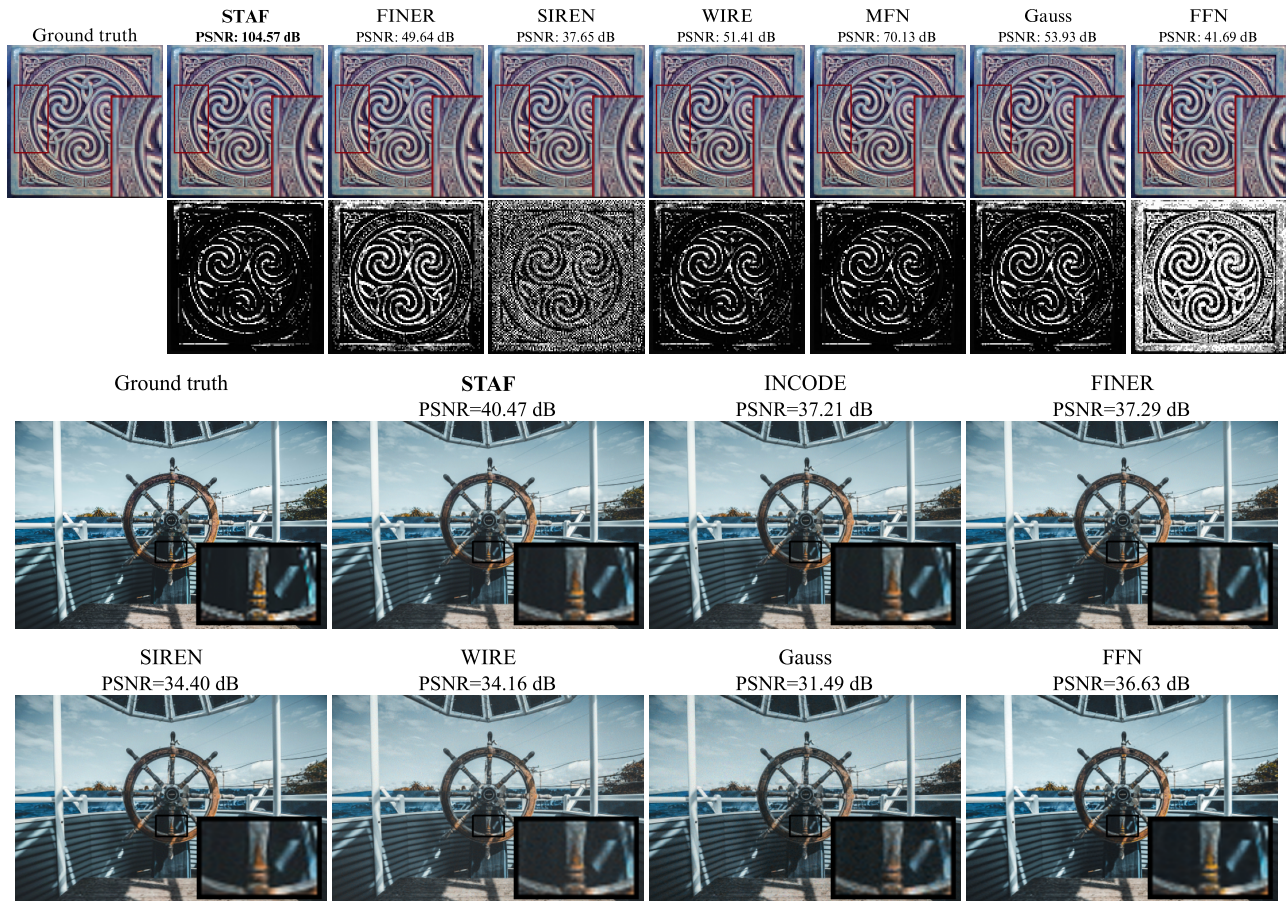


Figure 5. Comparative visualization of image representation using **STAF** and other activation functions. The second row highlights representation errors, with brighter areas indicating higher errors. The Celtic image size is 128×128 , and the second image from the DIV2K (Timofte et al., 2018) dataset is downsampled by a factor of $1/4$ to 510×339 .

an MLP architecture with 3 hidden layers and 256 hidden nodes. The models tested included INCODE, FINER, WIRE, Gauss, FFN, SIREN, ReLU with positional encoding, and MFN (Kazerouni et al., 2024; Liu et al., 2024b; Saragadam et al., 2023; Ramasinghe & Lucey, 2022; Sitzmann et al., 2020; Tancik et al., 2020; Fathy et al., 2020). We compared our approach with the recently proposed KAN networks (Liu et al., 2024a), particularly using the Chebyshev-Polynomial KAN variant, which provides a more efficient implementation of KAN networks (SS et al., 2024). All experiments were conducted on a desktop PC equipped with 32 GB of RAM and an NVIDIA RTX-3090 GPU. Our implementation was inspired by the codebases of SIREN, WIRE, and INCODE. The learning rates for each model were selected based on the optimal configurations reported in their original papers and codebases. For STAF, we used a learning rate of 2.5×10^{-4} . All models were trained with the Adam optimizer to ensure consistency in optimization and comparison. STAF was initialized using the methodology outlined in Section 3.5, specifically designed to enhance convergence and performance. Other models

were initialized following the strategies recommended in their respective original papers. We used $\tau = 5$ for all tasks, except image denoising ($\tau = 2$). Notably, we included a detailed Neural Tangent Kernel (NTK) analysis of our model (see Appendix A) and ablation studies in Appendix 6.

4.1. Signal Representations

We evaluated image representation tasks on several images, as shown in Figures 5 and Figure 7. STAF achieved the highest PSNR (104.57 dB) in the Celtic image task, outperforming SIREN (37.65 dB), WIRE (51.41 dB), and MFN (70.13 dB), with error maps highlighting its superior accuracy. In the larger-scale reconstruction task, STAF again led with 40.47 dB, surpassing INCODE (37.21 dB), FINER (37.29 dB), SIREN (34.40 dB), and others, as evident in the visual details and magnified insets. Figure 2 shows activation maps learned during the image reconstruction task. STAF produces more detailed and higher-quality reconstructions compared to SIREN and WIRE, highlighting its ability to capture complex features more effectively. We

also illustrate the performance comparison on a grayscale cameraman image in Figure 3 and the convergence rate of STAF in Figure 4, demonstrating STAF’s effectiveness in addressing the capacity-convergence gap in INR models (Liu et al., 2024b).

The quantitative and qualitative results of the shape representation are shown in Table 1 and Figure 9. Using the Stanford 3D Scanning Repository and following the INODE strategy (Kazerouni et al., 2024), we generated an occupancy volume by sampling points on a grid $512 \times 512 \times 512$, assigning 1 to voxels inside the object and 0 outside. The results demonstrate STAF’s capability to effectively capture both fine and coarse 3D shape details, achieving higher Intersection over Union (IoU) than other methods.

Table 1. Quantitative comparisons of SDF representations.

Methods	Armadillo	Dragon	Lucy	Thai Statue	Avg.
ReLU+PE.	0.9958	0.9966	0.9920	0.9911	0.9939
SIREN	0.9962	0.9971	0.9892	0.9929	0.9939
WIRE	0.9721	0.9749	0.9554	0.9507	0.9633
FINER	0.9965	0.9958	0.9962	0.9923	0.9952
INCODE	0.9849	0.9869	0.9774	0.9760	0.9813
STAF	0.9972	0.9973	0.9971	0.9935	0.9963

For the audio task, we used a 7-second clip from Bach’s Cello Suite No. 1: Prelude (Sitzmann et al., 2020), sampled at 44,100 Hz. Figure 8 illustrates the waveforms and reconstruction errors, where STAF demonstrates the highest PSNR, the lowest reconstruction error, and superior fidelity.

4.2. Inverse Problems

The results in Figure 10 and Figure 11 demonstrate that STAF consistently outperforms other activation-based implicit models in both super-resolution and image denoising tasks. INRs, when applied as interpolants, exhibit inherent biases that can be leveraged for inverse problems, particularly super-resolution. To validate this, we conducted $4 \times$ super-resolution experiments, where STAF achieved the highest PSNR (30.54 dB) and SSIM (0.89), surpassing the second-best INCODE (29.88 dB) and third-best FFN (29.41 dB). Other activations, such as SIREN and FINER, recover textures reasonably well but struggle with high-frequency details, while Gauss suffers from excessive blurring. These results indicate that STAF effectively reconstructs fine details, outperforming other INRs in high-resolution image recovery. For image denoising, we generated noisy images using realistic sensor measurements, introducing Poisson-distributed photon noise per pixel with a mean photon count of 10, simulating an extremely challenging low-light scenario with severe noise corruption. As shown in Figure 11, STAF achieves the highest PSNR (24.19 dB), demonstrating superior noise suppression and detail retention compared to other baselines. Methods such as FINER and FFN exhibit

noticeable artifacts, where the noise introduces proximity color distortions. These results confirm that STAF is effective in inverse problem tasks.

5. Expressive Power

In this part, we examine the expressive power of our architecture, drawing upon the notable Theorem 1 from (Yüce et al., 2022). This theorem is as follows:

Theorem 5.1. (Theorem 1 of (Yüce et al., 2022)) *Let $f_\theta : \mathbb{R}^D \rightarrow \mathbb{R}$ be an INR of the form of Equation (1) with $\rho^{(l)}(x) = \sum_{j=0}^J \alpha_j x^j$ for $l > 1$. Furthermore, let $\Psi = [\Psi_1, \dots, \Psi_T]^{tr} \in \mathbb{R}^{T \times D}$ and $\zeta \in \mathbb{R}^T$ denote the matrix of frequencies and vector of phases, respectively, used to map the input coordinate $r \in \mathbb{R}^D$ to $\gamma(r) = \sin(\Psi r + \zeta)$. This architecture can only represent functions of the form*

$$f_\theta(r) = \sum_{w' \in \mathcal{H}(\Psi)} c_{w'} \sin(\langle w', r \rangle + \zeta_{w'}),$$

where

$$\mathcal{H}(\Psi) \subseteq \tilde{\mathcal{H}}(\Psi) = \left\{ \sum_{t=1}^T s_t \Psi_t \mid s_t \in \mathbb{Z} \wedge \sum_{t=1}^T |s_t| \leq J^{L-1} \right\}.$$

Please note the following remarks regarding this theorem:

Remark 5.2. We refer to $\tilde{\mathcal{H}}$ as the set of potential frequencies.

Remark 5.3. The expression $\sum_{t=1}^T s_t \Psi_t$ is equal to $\Psi^{tr} [s_1, \dots, s_T]^{tr}$. This representation is more convenient for our subsequent discussion, as we will be exploring the kernel of Ψ in the sequel.

Remark 5.4. In the context of SIREN, where $\rho^{(l)} = \sin$, the post-activation function of the first layer, $z^{(0)} = \sin(\omega_0(\mathbf{W}^{(0)} \mathbf{r} + \mathbf{b}^{(0)}))$, can be interpreted as $\gamma(\mathbf{r}) = \sin(\Psi \mathbf{r} + \zeta)$.

We will now investigate the significant enhancement in expressive power offered by the proposed activation function. To facilitate comparison with SIREN, we express our network using sin as the activation function.

Let us consider a neural network with a parametric activation function defined in (2). To represent our network using SIREN, we demonstrate that every post-activation function of our network from the second layer onwards (z^{l+1}) can be expressed using linear transformations and sine functions. Notably, the final post-activation function ($z^{(L-1)}$) can be constructed using SIREN, albeit requiring more neurons than STAF. In other words, our network can be described using a SIREN and some Kronecker products denoted by \otimes . This analysis resembles that provided in (Jagtap et al., 2022), with a slight difference in the settings of the paper. In (Jagtap et al., 2022), it was shown that an adaptive activation

function of the form

$$\rho^*(x) = \sum_{i=1}^{\tau} C_i \rho_i(\Omega_i x) \quad (10)$$

can be represented using a feed-forward neural network, where each layer has neurons with activation functions ρ_i . To align STAF with this theorem, we must have $\rho_i = \sin(\Omega_i x + \Phi_i)$. However, here we aim to represent STAF using an architecture that only employs sine activation functions (SIREN). For this purpose, we introduce the following theorem, which holds true for every parametric activation function:

Theorem 5.5. *Let $L \geq 2$ and $1 \leq l \leq L$. Consider a neural network as defined in (1) with L layers. In addition, let $\Omega = [\Omega_1, \dots, \Omega_\tau]^{tr}$, $\Phi = [\Phi_1, \dots, \Phi_\tau]^{tr}$, and $C = [C_1, \dots, C_\tau]^{tr}$. If the trainable activation function is $\rho^*(x) = \sum_{m=1}^{\tau} C_m \rho(\Omega_m x + \Phi_m)$, then an equivalent neural network with activation function $\rho(x)$ and $L + 1$ layers can be constructed as follows (parameters of the equivalent network are denoted with an overline):*

$$\begin{aligned} \overline{\mathbf{z}}^{(0)} &= \gamma(\mathbf{r}), \\ \overline{\mathbf{z}}^{(l)} &= \rho\left(\overline{\mathbf{W}}^{(l)} \overline{\mathbf{z}}^{(l-1)} + \overline{\mathbf{B}}^{(l)}\right), \quad l = 1, \dots, L, \\ \overline{f}_{\overline{\theta}}(\mathbf{r}) &= \overline{\mathbf{W}}^{(L+1)} \overline{\mathbf{z}}^{(L)}; \end{aligned} \quad (11)$$

where

$$\overline{\mathbf{W}}^{(l)} = \begin{cases} \Omega \otimes \mathbf{W}^{(l)}, & \text{if } l = 1, \\ (\Omega \otimes C^{tr}) \otimes \mathbf{W}^{(l)}, & \text{if } l \text{ is even,} \\ (\Omega \otimes \mathbf{W}^{(l)}) (C^{tr} \otimes \mathbf{I}_{F_{l-1}}), & \text{if } l \text{ is odd, } l > 1, \text{ and } l \neq L + 1, \\ C^{tr} \otimes \mathbf{I}_{F_{l-1}}, & \text{if } l \text{ is odd, } l > 1, \text{ and } l = L + 1. \end{cases} \quad (12)$$

and

$$\overline{\mathbf{B}}^{(l)} = \Phi \otimes \mathbf{J}_{F_l}. \quad (13)$$

in which \mathbf{J}_{F_l} is an all-ones $F_l \times 1$ vector. Furthermore, if L is even, then $\overline{f}_{\overline{\theta}}(\mathbf{r}) = f_{\theta}(\mathbf{r})$ (we call these networks ‘Kronecker equivalent’ in this sense).

The proof of this theorem is provided in the Appendix C.2. As we observed, although a network with the activation function ρ^* can be represented using the activation function ρ , it features a unique architecture. These networks are not merely typical MLPs with the activation function ρ , as the weights in the Kronecker equivalent network exhibit dependencies due to the Kronecker product.

It is desirable that Theorem (5.5) does not depend on the parity of L . To achieve this, consider the following remark:

Remark 5.6. We can introduce a dummy layer with the activation function ρ^* . Specifically, we define $\mathbf{z}^{(L)} = \rho^*(f_{\theta}(\mathbf{r}))$, and $\overline{f}_{\overline{\theta}}(\mathbf{r}) = \overline{\mathbf{W}}^{(L+1)} \mathbf{z}^{(L)} + \overline{\mathbf{B}}^{(L+1)}$, where

$\overline{\mathbf{W}}^{(L+1)} = \mathbf{O}$. To ensure that $\overline{f}_{\overline{\theta}}(\mathbf{r}) = f_{\theta}(\mathbf{r})$, we set $\overline{\mathbf{B}}^{(L+1)} = f_{\theta}(\mathbf{r})$. This approach allows us to construct an equivalent neural network with one more layer.

As a result of Remark (5.6), the equivalent network of a network with a trainable activation function, has either one more layer, or the same number of layers. As an immediate result of Theorem (5.5), if we denote the embedding of the first layer of the SIREN equivalent of our network by $\overline{\Psi}$, then

$$\overline{\Psi} = \overline{\mathbf{W}}^{(1)} = \Omega \otimes \mathbf{W}^{(1)} \in \mathbb{R}^{\tau F_1 \times F_0} \quad (14)$$

which is τ times bigger than the embedding of the first layer of a SIREN with $\mathbf{W}^{(1)} \in \mathbb{R}^{F_1 \times F_0}$. To understand the impact of this increase on expressive power, it suffices to substitute T with τT in Theorem (5.1). The next theorem will reveal how this change will affect the cardinality of the set of potential frequencies.

Theorem 5.7. (Page 4 of (Kiselman, 2012)) *Let $V(T, K) = \{(s_1, s_2, \dots, s_T) \in \mathbb{Z}^T \mid \sum_{t=1}^T |s_t| \leq K\}$.¹ Then we have*

$$|V(T, K)| = \sum_{i=0}^{\min(K, T)} \binom{i}{K} \binom{i}{T} 2^i \quad (15)$$

This number is called Delannoy number. Moreover, for fixed K ,

$$|V(T, K)| \sim A_K (2T)^K, \quad T \rightarrow +\infty \quad (16)$$

As an immediate result of this theorem, for large values of T ,

$$\frac{|V(\tau T, K)|}{|V(T, K)|} \sim \tau^K \quad (17)$$

Now, it is time to analyze the cardinality of the set of potential frequencies:

$$\tilde{\mathcal{H}}(\Psi) = \left\{ \sum_{t=1}^T s_t \Psi_t \mid (s_1, s_2, \dots, s_T) \in V(T, J^{L-1}) \right\} \quad (18)$$

or equivalently,

$$\tilde{\mathcal{H}}(\Psi) = \left\{ \Psi^{tr} [s_1, \dots, s_T]^{tr} \mid s_t \in \mathbb{Z} \wedge \sum_{t=1}^T |s_t| \leq J^{L-1} \right\} \quad (19)$$

The cardinality of the set $\tilde{\mathcal{H}}(\Psi)$ is bounded above by $V(T, J^{L-1})$. If Ψ^{tr} is injective on the integer lattice \mathbb{Z}^T , then $|\tilde{\mathcal{H}}(\Psi)| = |V(T, J^{L-1})|$. However, in general, analyzing how a linear transformation affects the size of a convex body can be approached using the geometry of numbers (Matousek, 2013) or additive geometry (Tao & Vu, 2006).

¹ We use V to denote these points as cells in a T -dimensional von Neumann neighborhood of K , clarifying that V does not represent a vector space.

To simplify the analysis and preserve the size of $\tilde{\mathcal{H}}(\Psi)$ as large as possible, we can slightly perturb the matrix Ψ^{tr} such that its kernel contains no points with rational coordinates, except the origin. This is a much stronger condition than having no integer lattice points in the kernel. To address this, we introduce a lemma. It’s worth noting that we can assume the matrices are stored with rational entries, as they are typically represented in computers using floating-point numbers. In our subsequent analysis, however, assuming rational entries for just one column of the matrix Ψ is sufficient.

Lemma 5.8. *Let $A \in \mathbb{R}^{D \times T}$, and for one of its rows, like r ’th row, we have $A_r \in \mathbb{Q}^T$. Then, in every neighborhood of A , there is a matrix \hat{A} such that $\text{Ker}(\hat{A}) \cap \mathbb{Q}^T = \mathbf{O}$.*

(The proof is provided in the Appendix C.3.) Consider Lemma (5.8), where we let $A = \Psi^{tr}$. Thus, for every neighborhood of Ψ^{tr} , there exists a matrix $\hat{\Psi}^{tr}$ such that $\text{Ker}(\hat{\Psi}^{tr}) \cap \mathbb{Q}^T = \mathbf{O}$; in other words, $\hat{\Psi}^{tr}$ is injective over rational points, and consequently over integer lattice points. This guarantees that $|\tilde{\mathcal{H}}(\hat{\Psi})| = |V(T, J^{L-1})|$.

In summary, this section demonstrated that, in comparison to SIREN, STAF can substantially increase the size of the set of potential frequencies by a factor of τ^K . This underscores how leveraging the properties of the Kronecker product enables the proposed activation function to significantly enhance expressive power.

6. Conclusion

In this paper, we introduced STAF as a novel approach to enhancing INRs. Our work mitigates the limitations of conventional ReLU neural networks, particularly their spectral bias which impedes the reconstruction of fine details in target signals. Through experimentation, we demonstrated that STAF significantly outperforms SOTA models like FINER, INCODE, and Fourier features in terms of accuracy, convergence speed, and PSNR value. Our results demonstrate the effectiveness of STAF in capturing high-frequency details more precisely, which is crucial for applications in computer graphics and data compression. The parametric, trainable nature of STAF allows for adaptive learning tailored to the specific characteristics of the input signals, resulting in superior reconstruction quality. Moreover, our theoretical analysis provided insights into the underlying mechanisms that contribute to the improved performance of STAF. By combining the strengths of the Fourier series with the flexibility of neural networks, STAF presents a powerful tool for various high-fidelity signal processing tasks.

Impact Statement

This paper presents work whose goal is to advance the field of neural representations. There are many potential societal consequences of our work, none of which we feel must be specifically highlighted here.

References

- Aftab, A., Morsali, A., and Ghaemmaghami, S. Multi-head relu implicit neural representation networks. In *ICASSP 2022-2022 IEEE International Conference on Acoustics, Speech and Signal Processing (ICASSP)*, pp. 2510–2514. IEEE, 2022.
- Albrecht, K., Entzian, J., and Iske, A. Product kernels are efficient and flexible tools for high-dimensional scattered interpolation. *ArXiv*, abs/2312.09949, 2023. URL <https://api.semanticscholar.org/CorpusID:266335528>.
- Ashendorf, T., Wong, F., Eils, R., and Gunawardena, J. A framework for modelling gene regulation which accommodates non-equilibrium mechanisms: Additional file 1. Supplementary material to the article published in *BMC Biology*, Dec 2014. Available at <https://vcp.med.harvard.edu/papers/jg-genex-supp.pdf>.
- Bai, J., Liu, G.-R., Gupta, A., Alzubaidi, L., Feng, X.-Q., and Gu, Y. Physics-informed radial basis network (PIRBN): A local approximating neural network for solving nonlinear partial differential equations. *Computer Methods in Applied Mechanics and Engineering*, 415: 116290, 2023.
- Barron, J. T., Mildenhall, B., Verbin, D., Srinivasan, P. P., and Hedman, P. Zip-nerf: Anti-aliased grid-based neural radiance fields. In *Proceedings of the IEEE/CVF International Conference on Computer Vision*, pp. 19697–19705, 2023.
- Biswas, K., Kumar, S., Banerjee, S., and Pandey, A. K. Tanhsoft—dynamic trainable activation functions for faster learning and better performance. *IEEE Access*, 9:120613–120623, 2021.
- Braun, M. L. *Spectral properties of the kernel matrix and their relation to kernel methods in machine learning*. PhD thesis, Universitäts- und Landesbibliothek Bonn, 2005.
- Chen, Y., Liu, S., and Wang, X. Learning continuous image representation with local implicit image function. In *Proceedings of the IEEE/CVF conference on computer vision and pattern recognition*, pp. 8628–8638, 2021.
- Chen, Y., Wu, Q., Harandi, M., and Cai, J. How far can we compress instant-ngp-based NeRF? In *Proceedings of the IEEE/CVF Conference on Computer Vision and Pattern Recognition*, pp. 20321–20330, 2024.
- Chen, Z., Shi, X., Rudner, T. G., Feng, Q., Zhang, W., and Zhang, T. A neural tangent kernel perspective on function-space regularization in neural networks. In *OPT 2022: Optimization for Machine Learning (NeurIPS 2022 Workshop)*, 2022.

- Churchill, E. Information given by odd moments. *Ann. Math. Stat.*, 17(2):244–246, 1946.
- Elfwing, S., Uchibe, E., and Doya, K. Sigmoid-weighted linear units for neural network function approximation in reinforcement learning. *Neural Networks*, 107:3–11, 2018.
- Fathony, R., Sahu, A. K., Willmott, D., and Kolter, J. Z. Multiplicative filter networks. In *International Conference on Learning Representations*, 2020.
- Gallant, A. R. and White, H. There exists a neural network that does not make avoidable mistakes. In *ICNN*, pp. 657–664, 1988.
- Ghojogh, B., Ghodsi, A., Karray, F., and Crowley, M. Reproducing kernel hilbert space, mercer’s theorem, eigenfunctions, nyström method, and use of kernels in machine learning: Tutorial and survey. *arXiv preprint arXiv:2106.08443*, 2021.
- Golikov, E., Pokonechnyy, E., and Korviakov, V. Neural tangent kernel: A survey. *arXiv preprint arXiv:2208.13614*, 2022.
- Hendrycks, D. and Gimpel, K. Gaussian error linear units (gelus). *arXiv preprint arXiv:1606.08415*, 2016.
- Jacot, A., Gabriel, F., and Hongler, C. Neural tangent kernel: Convergence and generalization in neural networks. *Advances in neural information processing systems*, 31, 2018.
- Jagtap, A. D., Shin, Y., Kawaguchi, K., and Karniadakis, G. E. Deep kronecker neural networks: A general framework for neural networks with adaptive activation functions. *Neurocomputing*, 468:165–180, 2022.
- Kadarvish, M. S., Mojtahedi, H., Zarch, H. E., Kazerooni, A., Morsali, A., Abtahi, A., and Marvasti, F. Ensemble neural representation networks. *arXiv preprint arXiv:2110.04124*, 2021.
- Kazerooni, A., Azad, R., Hosseini, A., Merhof, D., and Bagci, U. INCODE: Implicit neural conditioning with prior knowledge embeddings. In *Proceedings of the IEEE/CVF Winter Conference on Applications of Computer Vision*, pp. 1298–1307, 2024.
- Kiselman, C. Asymptotic properties of the delannoy numbers and similar arrays. *Preprint*, pp. 5–6, 2012.
- Lapedes, A. and Farber, R. Nonlinear signal processing using neural networks: Prediction and system modelling. Technical report, 1987.
- Li, R., Fidler, S., Kanazawa, A., and Williams, F. Nerf-xl: Scaling nerfs with multiple gpus. In *European Conference on Computer Vision*, pp. 92–107. Springer, 2025.
- Liao, Z. Trainable activation function in image classification. *arXiv preprint arXiv:2004.13271*, 2020.
- Lin, C.-Y., Fu, Q., Merth, T., Yang, K., and Ranjan, A. Fastsr-nerf: Improving nerf efficiency on consumer devices with a simple super-resolution pipeline. In *Proceedings of the IEEE/CVF Winter Conference on Applications of Computer Vision*, pp. 6036–6045, 2024.
- Liu, Z., Wang, Y., Vaidya, S., Ruehle, F., Halverson, J., Soljačić, M., Hou, T. Y., and Tegmark, M. KAN: Kolmogorov-arnold networks. *arXiv preprint arXiv:2404.19756*, 2024a.
- Liu, Z., Zhu, H., Zhang, Q., Fu, J., Deng, W., Ma, Z., Guo, Y., and Cao, X. FINER: Flexible spectral-bias tuning in implicit neural representation by variable-periodic activation functions. In *Proceedings of the IEEE/CVF Conference on Computer Vision and Pattern Recognition*, pp. 2713–2722, 2024b.
- Maas, A. L., Hannun, A. Y., Ng, A. Y., et al. Rectifier nonlinearities improve neural network acoustic models. In *Proc. icml*, volume 30, pp. 3. Citeseer, 2013.
- Martel, J. N., Lindell, D. B., Lin, C. Z., Chan, E. R., Monteiro, M., and Wetzstein, G. Acorn: Adaptive coordinate networks for neural scene representation. *arXiv preprint arXiv:2105.02788*, 2021.
- Matousek, J. *Lectures on discrete geometry*, volume 212. Springer Science & Business Media, 2013.
- Mehta, I., Gharbi, M., Barnes, C., Shechtman, E., Ramamoorthi, R., and Chandraker, M. Modulated periodic activations for generalizable local functional representations. In *Proceedings of the IEEE/CVF International Conference on Computer Vision*, pp. 14214–14223, 2021.
- Mescheder, L., Oechsle, M., Niemeyer, M., Nowozin, S., and Geiger, A. Occupancy networks: Learning 3d reconstruction in function space. In *Proceedings of the IEEE/CVF conference on computer vision and pattern recognition*, pp. 4460–4470, 2019.
- Mildenhall, B., Srinivasan, P. P., Tancik, M., Barron, J. T., Ramamoorthi, R., and Ng, R. NeRF: Representing scenes as neural radiance fields for view synthesis. In *ECCV*, 2020.
- Mohamadi, M. A., Bae, W., and Sutherland, D. J. A fast, well-founded approximation to the empirical neural tangent kernel. In *International Conference on Machine Learning*, pp. 25061–25081. PMLR, 2023.

- Müller, T., Evans, A., Schied, C., and Keller, A. Instant neural graphics primitives with a multiresolution hash encoding. *ACM Trans. Graph.*, 41(4):102:1–102:15, July 2022. doi: 10.1145/3528223.3530127. URL <https://doi.org/10.1145/3528223.3530127>.
- Nair, V. and Hinton, G. E. Rectified linear units improve restricted boltzmann machines. In *Icml*, 2010.
- Novak, R., Xiao, L., Hron, J., Lee, J., Alemi, A. A., Sohl-Dickstein, J., and Schoenholz, S. S. Neural tangents: Fast and easy infinite neural networks in python. *arXiv preprint arXiv:1912.02803*, 2019.
- Parascandolo, G., Huttunen, H., and Virtanen, T. Taming the waves: sine as activation function in deep neural networks. 2016.
- Paul, A., Bandyopadhyay, R., Yoon, J. H., Geem, Z. W., and Sarkar, R. Sinlu: Sinu-sigmoidal linear unit. *Mathematics*, 10(3):337, 2022.
- Radhakrishnan, A. Modern machine learning: Simple methods that work, 2024. Lectures 5 and 6, available at <https://web.mit.edu/modernml/course/>.
- Rahaman, N., Baratin, A., Arpit, D., Draxler, F., Lin, M., Hamprecht, F., Bengio, Y., and Courville, A. On the spectral bias of neural networks. In *International Conference on Machine Learning*, pp. 5301–5310. PMLR, 2019.
- Ramachandran, P., Zoph, B., and Le, Q. V. Searching for activation functions. *arXiv preprint arXiv:1710.05941*, 2017.
- Ramasinghe, S. and Lucey, S. Beyond periodicity: Towards a unifying framework for activations in coordinate-mlps. In *European Conference on Computer Vision*, pp. 142–158. Springer, 2022.
- Reiser, C., Peng, S., Liao, Y., and Geiger, A. Kilonerf: Speeding up neural radiance fields with thousands of tiny mlps. In *Proceedings of the IEEE/CVF International Conference on Computer Vision*, pp. 14335–14345, 2021.
- Saragadam, V., Tan, J., Balakrishnan, G., Baraniuk, R. G., and Veeraraghavan, A. MINER: Multiscale implicit neural representation. In *European Conference on Computer Vision*, pp. 318–333. Springer, 2022.
- Saragadam, V., LeJeune, D., Tan, J., Balakrishnan, G., Veeraraghavan, A., and Baraniuk, R. G. WIRE: Wavelet implicit neural representations. In *Proceedings of the IEEE/CVF Conference on Computer Vision and Pattern Recognition*, pp. 18507–18516, 2023.
- Shiryayev, A. N. *Probability-1*. Graduate Texts in Mathematics. Springer, New York, NY, 3 edition, July 2016.
- Shivappriya, S., Priyadarsini, M. J. P., Stateczny, A., Puttamadappa, C., and Parameshachari, B. Cascade object detection and remote sensing object detection method based on trainable activation function. *Remote Sensing*, 13(2):200, 2021.
- Sitzmann, V., Martel, J., Bergman, A., Lindell, D., and Wetzstein, G. Implicit neural representations with periodic activation functions. *Advances in Neural Information Processing Systems*, 33:7462–7473, 2020.
- SS, S. et al. Chebyshev polynomial-based kolmogorov-arnold networks: An efficient architecture for nonlinear function approximation. *arXiv e-prints*, pp. arXiv–2405, 2024.
- Stewart, I. *Galois Theory*. Chapman and Hall/CRC, 2022. Exercise 6.10.
- Tancik, M., Srinivasan, P., Mildenhall, B., Fridovich-Keil, S., Raghavan, N., Singhal, U., Ramamoorthi, R., Barron, J., and Ng, R. Fourier features let networks learn high frequency functions in low dimensional domains. *Advances in Neural Information Processing Systems*, 33: 7537–7547, 2020.
- Tao, T. and Vu, V. H. *Additive combinatorics*, volume 105. Cambridge University Press, 2006.
- Timofte, R., Gu, S., Wu, J., Van Gool, L., Zhang, L., Yang, M.-H., Haris, M., Shakhnarovich, G., Ukita, N., Hu, S., Bei, Y., Hui, Z., Jiang, X., Gu, Y., Liu, J., Wang, Y., Perazzi, F., McWilliams, B., Sorkine-Hornung, A., Sorkine-Hornung, O., Schroers, C., Yu, J., Fan, Y., Yang, J., Xu, N., Wang, Z., Wang, X., Huang, T. S., Wang, X., Yu, K., Hui, T.-W., Dong, C., Lin, L., Change Loy, C., Park, D., Kim, K., Chun, S. Y., Zhang, K., Liu, P., Zuo, W., Guo, S., Liu, J., Xu, J., Liu, Y., Xiong, F., Dong, Y., Bai, H., Damian, A., Ravi, N., Menon, S., Rudin, C., Seo, J., Jeon, T., Koo, J., Jeon, S., Kim, S. Y., Choi, J.-S., Ki, S., Seo, S., Sim, H., Kim, S., Kim, M., Chen, R., Zeng, K., Guo, J., Qu, Y., Li, C., Ahn, N., Kang, B., Sohn, K.-A., Yuan, Y., Zhang, J., Pang, J., Xu, X., Zhao, Y., Deng, W., Ul Hussain, S., Aadil, M., Rahim, R., Cai, X., Huang, F., Xu, Y., Michelini, P. N., Zhu, D., Liu, H., Kim, J.-H., Lee, J.-S., Huang, Y., Qiu, M., Jing, L., Zeng, J., Wang, Y., Sharma, M., Mukhopadhyay, R., Upadhyay, A., Koundinya, S., Shukla, A., Chaudhury, S., Zhang, Z., Hu, Y. H., and Fu, L. NTIRE 2018 challenge on single image super-resolution: Methods and results. In *2018 IEEE/CVF Conference on Computer Vision and Pattern Recognition Workshops (CVPRW)*, pp. 965–96511, 2018. doi: 10.1109/CVPRW.2018.00130.
- Uy, M. A., Nakayama, K., Yang, G., Thomas, R., Guibas, L. J., and Li, K. Nerf revisited: Fixing quadrature instabil-

ity in volume rendering. *Advances in Neural Information Processing Systems*, 36, 2024.

Wang, H., Lu, L., Song, S., and Huang, G. Learning specialized activation functions for physics-informed neural networks. *arXiv preprint arXiv:2308.04073*, 2023.

Wang, S., Yu, X., and Perdikaris, P. When and why PINNs fail to train: A neural tangent kernel perspective. *Journal of Computational Physics*, 449:110768, 2022.

Williams, C. and Seeger, M. The effect of the input density distribution on kernel-based classifiers. In *ICML'00 Proceedings of the Seventeenth International Conference on Machine Learning*, pp. 1159–1166. Morgan Kaufmann Publishers Inc., 2000.

Xu, X., Yang, Y., Mo, K., Pan, B., Yi, L., and Guibas, L. JacobiNeRF: Nerf shaping with mutual information gradients. In *Proceedings of the IEEE/CVF Conference on Computer Vision and Pattern Recognition*, pp. 16498–16507, 2023.

Yüce, G., Ortiz-Jiménez, G., Besbinar, B., and Frossard, P. A structured dictionary perspective on implicit neural representations. In *Proceedings of the IEEE/CVF Conference on Computer Vision and Pattern Recognition*, pp. 19228–19238, 2022.

Appendix

Table of Contents

A Neural Tangent Kernel	14
A.1 Analytic NTK	14
A.2 Proof of Lemma (A.3)	18
B Ablation Studies	18
B.1 Impact of Amplitude, Frequency, and Phase	18
B.2 Comparative Analysis of Activation Strategies	18
B.3 Performance Comparison of STAF and SIREN with Similar Parameter Counts	19
B.4 More Comparative Evaluation	20
C Proofs	21
C.1 Proof of Theorem (3.1)	21
C.2 Proof of Theorem (5.5)	27
C.3 Proof of Lemma (5.8)	30

A. Neural Tangent Kernel

The Neural Tangent Kernel (NTK) is a significant concept in the theoretical understanding of neural networks, particularly in the context of their training dynamics (Jacot et al., 2018). To be self-contained, we provide an explanation of the NTK and its background in kernel methods. We believe this will be beneficial for readers, as previous papers on implicit neural representation using the NTK concept have not adequately explained the NTK or the significance of its eigenvalues and eigenfunctions.

A kernel is a function $K(\mathbf{x}, \tilde{\mathbf{x}})$ used in integral transforms to define an operator that maps a function f to another function T_f through the integral equation

$$T_f(\mathbf{x}) = \int K(\mathbf{x}, \tilde{\mathbf{x}})f(\tilde{\mathbf{x}}) d\tilde{\mathbf{x}}.$$

Since T_f is a linear operator with respect to f , we can discuss its eigenvalues and eigenfunctions. The eigenvalues and eigenfunctions of a kernel are the scalar values λ and the corresponding functions $\zeta(\mathbf{x})$ that satisfy the following equation (Ghojogh et al., 2021)

$$\int K(\mathbf{x}, \tilde{\mathbf{x}})\zeta(\tilde{\mathbf{x}}) d\tilde{\mathbf{x}} = \lambda\zeta(\mathbf{x}).$$

In the context of neural networks, the concept of a kernel becomes particularly remarkable when analyzing the network’s behavior in the infinite-width limit. Kernels in machine learning, such as the Radial Basis Function (RBF) kernel or polynomial kernel, are used to measure similarity between data points in a high-dimensional feature space. These kernels allow the application of linear methods to non-linear problems by implicitly mapping the input data into a higher-dimensional space (Braun, 2005).

The NTK extends this idea by considering the evolution of a neural network’s outputs during training. When a neural network is infinitely wide, its behavior can be closely approximated by a kernel method. In this case, the kernel in question is the NTK, which emerges from the first-order Taylor series approximation (or tangent plane approximation) of the network’s outputs.

Formally, for a neural network $f(\mathbf{x}; \boldsymbol{\theta})$ with input \mathbf{x} and parameters $\boldsymbol{\theta}$, the NTK, denoted as $K^{(L)}(\mathbf{x}, \tilde{\mathbf{x}})$, is defined as:

$$K^{(L)}(\mathbf{x}, \tilde{\mathbf{x}}) = \langle \nabla_{\boldsymbol{\theta}} f(\mathbf{x}; \boldsymbol{\theta}), \nabla_{\boldsymbol{\theta}} f(\tilde{\mathbf{x}}; \boldsymbol{\theta}) \rangle,$$

where $\nabla_{\boldsymbol{\theta}} f(\mathbf{x}; \boldsymbol{\theta})$ represents the gradient of the network output with respect to its parameters.

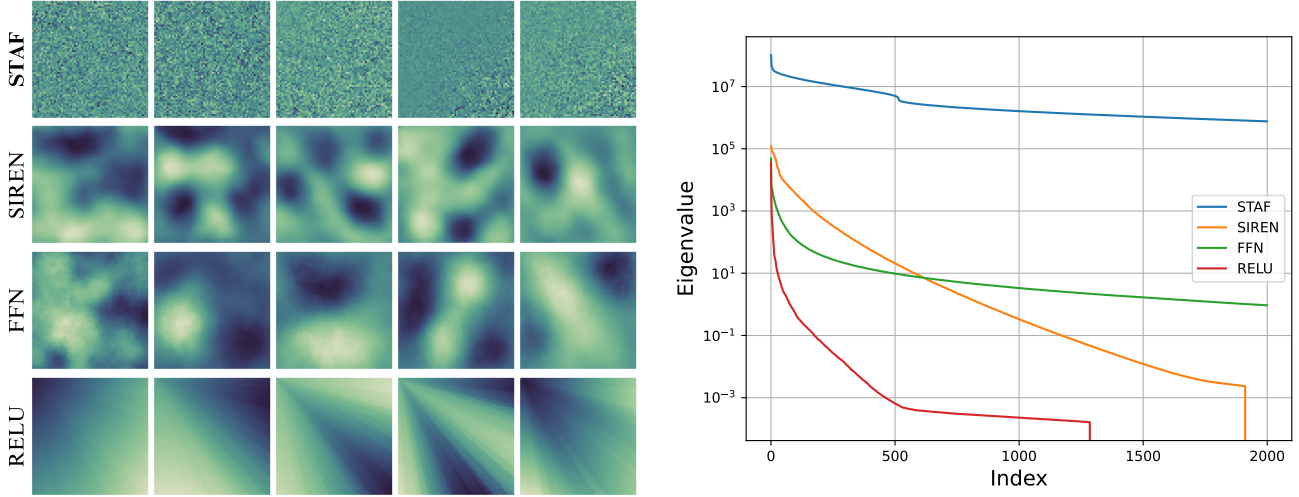
There are two methods for calculating the NTK: the analytic approach and the empirical approach (Novak et al., 2019; Chen et al., 2022). In the paper, we derived the analytic NTK of a neural network that uses our activation function, as detailed in the appendix. However, for our experimental purposes, we utilized the empirical NTK. It is worth noting that calculating the NTK for real-world networks is highly challenging, and typically not computationally possible (Mohamadi et al., 2023).

Just like the computation of NTK, there are analytic and empirical methods for calculating the eigenvalues and eigenfunctions of a kernel (Williams & Seeger, 2000). These values play a crucial role in characterizing neural network training. For instance, it has been shown that the eigenvalues of the NTK determine the convergence rate (Wang et al., 2022; Bai et al., 2023). Specifically, components of the target function associated with kernel eigenvectors having larger eigenvalues are learned faster (Wang et al., 2022; Tancik et al., 2020). In fully-connected networks, the eigenvectors corresponding to higher eigenvalues of the NTK matrix generally represent lower frequency components (Wang et al., 2022). Furthermore, the eigenfunctions of an NTK can illustrate how effectively a model learns a signal dictionary (Yüce et al., 2022).

Figure 6(a) illustrates the eigenfunctions of various NTKs using different activation functions. As shown, the STAF activation function results in finer eigenfunctions, which intuitively enhances the ability to learn and reconstruct higher frequency components. Additionally, Figure 6(b) presents the eigenvalues of different NTKs with various activation functions. The results indicate that STAF produces higher eigenvalues, leading to a faster convergence rate during training. Moreover, STAF also generates a greater number of eigenvalues, compared to ReLU and SIREN. Having more eigenvalues is beneficial because it suggests a richer and more expressive kernel, capable of capturing a wider range of features and details in the data.

A.1. Analytic NTK

In this section, we compute the analytic NTK for a neural network that uses the proposed activation function (STAF), following the notation from (Radhakrishnan, 2024). Interested readers can also refer to (Jacot et al., 2018) and (Golikov et al.,



(a) The first five eigenfunctions of the empirical NTK of STAF, SIREN, FFN, and ReLU.

(b) The eigenvalue spectrum of the empirical NTK of STAF, SIREN, FFN, and ReLU.

Figure 6. (a) The first five eigenfunctions of the empirical NTK of STAF, SIREN, FFN, and ReLU. (b) The eigenvalue spectrum of the empirical NTK of STAF, SIREN, FFN, and ReLU.

2022). However, we chose (Radhakrishnan, 2024) for its clarity and ease of understanding. According to (Radhakrishnan, 2024), the NTK of an activation function for a neural network with $L - 1$ hidden layers is as follows.

Theorem A.1. (Theorem 1 of (Radhakrishnan, 2024), Lecture 6) For $\mathbf{x} \in S^{d-1}$, let $f_{\mathbf{x}}^{(L)}(\mathbf{w}) : \mathbb{R}^p \rightarrow \mathbb{R}$ denote a neural network with $L - 1$ hidden layers such that:

$$f_{\mathbf{x}}^{(L)}(\mathbf{w}) = \mathbf{W}^{(L)} \frac{1}{\sqrt{F_{L-1}}} \phi \left(\mathbf{W}^{(L-1)} \frac{1}{\sqrt{F_{L-2}}} \phi \left(\dots \mathbf{W}^{(2)} \frac{1}{\sqrt{F_1}} \phi \left(\mathbf{W}^{(1)} \mathbf{x} \right) \dots \right) \right); \quad (20)$$

where $W^{(i)} \in \mathbb{R}^{F_i \times F_{i-1}}$ for $i \in \{1, \dots, L\}$ with $F_0 = d$, $F_L = 1$, and $\phi : \mathbb{R} \rightarrow \mathbb{R}$ is an element-wise activation function. As $F_1, F_2, \dots, F_{L-1} \rightarrow \infty$ in order, the Neural Network Gaussian Process (NNGP), denoted as $\Sigma^{(L)}$, and the NTK, denoted as $K^{(L)}$, of $f_{\mathbf{x}}(\mathbf{w})$ are given by:

$$\begin{aligned} \Sigma^{(L)}(\mathbf{x}, \tilde{\mathbf{x}}) &= \check{\phi} \left(\Sigma^{(L-1)}(\mathbf{x}, \tilde{\mathbf{x}}) \right); & \Sigma^{(0)}(\mathbf{x}, \tilde{\mathbf{x}}) &= \mathbf{x}^T \tilde{\mathbf{x}} \\ K^{(L)}(\mathbf{x}, \tilde{\mathbf{x}}) &= \Sigma^{(L)}(\mathbf{x}, \tilde{\mathbf{x}}) + K^{(L-1)}(\mathbf{x}, \tilde{\mathbf{x}}) \check{\phi}' \left(\Sigma^{(L-1)}(\mathbf{x}, \tilde{\mathbf{x}}) \right); \\ K^{(0)}(\mathbf{x}, \tilde{\mathbf{x}}) &= \mathbf{x}^T \tilde{\mathbf{x}} \end{aligned} \quad (21)$$

where $\check{\phi} : [-1, 1] \rightarrow \mathbb{R}$ is the dual activation for ϕ , and is calculated as follows:

$$\check{\phi}(\xi) = \mathbb{E}_{(u,v) \sim \mathcal{N}(0, \mathbf{\Lambda})} [\phi(u)\phi(v)] \quad \text{where } \mathbf{\Lambda} = \begin{bmatrix} 1 & \xi \\ \xi & 1 \end{bmatrix}. \quad (22)$$

Furthermore, ϕ is normalized such that $\check{\phi}(1) = 1$.

Consequently, it suffices to calculate $\check{\phi}$. It has been calculated in the following theorem. Just like what mentioned in (Wang et al., 2023), we assume that the optimization of neural networks with STAF can be decomposed into two phases, where we learn the coefficients of STAF in the first phase and then train the parameters of neural network in the second phase. This assumption is reasonable as the number of parameters of STAF is far less than those of networks and they quickly converge at the early stage of training. As a result, in the following theorem, all the parameters except weights are fixed, since they have been obtained in the first phase of training.

Theorem A.2. Let ρ^* be the proposed activation function (STAF). Then

$$\begin{aligned}\check{\rho}^*(\xi) &= \sum_{i=1}^{\tau} \sum_{j=1}^{\tau} C_i C_j \Delta_{i,j} \\ &= \frac{1}{2} \sum_{i=1}^{\tau} \sum_{j=1}^{\tau} C_i C_j e^{\frac{-1}{2}(\Omega_i^2 + \Omega_j^2)} \left(e^{\Omega_i \Omega_j \xi} \cos(\Phi_i - \Phi_j) + e^{-\Omega_i \Omega_j \xi} \cos(\Phi_i + \Phi_j) \right)\end{aligned}\quad (23)$$

Therefore,

$$\check{\rho}^{*\prime}(\xi) = \frac{1}{2} \sum_{i=1}^{\tau} C_i \Omega_i \sum_{j=1}^{\tau} \left[C_j \Omega_j e^{\frac{-1}{2}(\Omega_i^2 + \Omega_j^2)} \left(e^{\Omega_i \Omega_j \xi} \cos(\Phi_i - \Phi_j) - e^{-\Omega_i \Omega_j \xi} \cos(\Phi_i + \Phi_j) \right) \right]. \quad (24)$$

Proof.

$$\begin{aligned}\check{\rho}^*(\xi) &= \mathbb{E}_{(u,v) \sim \mathcal{N}(0,\mathbf{\Lambda})} [\rho^*(u) \rho^*(v)] \\ &= \mathbb{E}_{(u,v) \sim \mathcal{N}(0,\mathbf{\Lambda})} \left[\sum_{i=1}^{\tau} C_i \sin(\Omega_i u + \Phi_i) \sum_{i=1}^{\tau} C_i \sin(\Omega_i v + \Phi_i) \right] \\ &= \mathbb{E}_{(u,v) \sim \mathcal{N}(0,\mathbf{\Lambda})} \left[\sum_{i=1}^{\tau} \sum_{j=1}^{\tau} C_i C_j \sin(\Omega_i u + \Phi_i) \sin(\Omega_j v + \Phi_j) \right] \\ &= \sum_{i=1}^{\tau} \sum_{j=1}^{\tau} C_i C_j \mathbb{E}_{(u,v) \sim \mathcal{N}(0,\mathbf{\Lambda})} \left(\sin(\Omega_i u + \Phi_i) \sin(\Omega_j v + \Phi_j) \right).\end{aligned}\quad (25)$$

So, we need to compute the following expectation:

$$\Delta_{i,j} = \mathbb{E}_{(u,v) \sim \mathcal{N}(0,\mathbf{\Lambda})} \left(\sin(\Omega_i u + \Phi_i) \sin(\Omega_j v + \Phi_j) \right) \quad (26)$$

Note that for a random vector $\mathbf{X} = (X_1, \dots, X_d)^T$ with mean vector $\boldsymbol{\mu}$ and covariance matrix $\mathbf{\Lambda}$, the joint probability density function (PDF) is as follows:

$$f_{\mathbf{X}}(\mathbf{x}) = (2\pi)^{-d/2} \det(\mathbf{\Lambda})^{-1/2} e^{\left(\frac{-1}{2}(\mathbf{x}-\boldsymbol{\mu})^T \mathbf{\Lambda}^{-1}(\mathbf{x}-\boldsymbol{\mu})\right)}. \quad (27)$$

As a result, since $\mathbf{\Lambda}^{-1} = \frac{1}{1-\xi^2} \begin{bmatrix} 1 & -\xi \\ -\xi & 1 \end{bmatrix}$, we will have:

$$\begin{aligned}f_{U,V}(u,v) &= \frac{1}{2\pi\sqrt{1-\xi^2}} e^{-\frac{1}{2}(u \ v) \mathbf{\Lambda}^{-1} \begin{pmatrix} u \\ v \end{pmatrix}} = \frac{1}{2\pi\sqrt{1-\xi^2}} e^{\frac{-1}{2(1-\xi^2)}(u \ v) \begin{pmatrix} 1 & -\xi \\ -\xi & 1 \end{pmatrix} \begin{pmatrix} u \\ v \end{pmatrix}} \\ &= \frac{1}{2\pi\sqrt{1-\xi^2}} e^{\frac{-(u^2 - 2\xi uv + v^2)}{2(1-\xi^2)}}.\end{aligned}\quad (28)$$

Consequently, using Equations (25) and (26), we have

$$\begin{aligned}\Delta_{i,j} &= \int_{-\infty}^{\infty} \int_{-\infty}^{\infty} \left(\sin(\Omega_i u + \Phi_i) \sin(\Omega_j v + \Phi_j) f_{U,V}(u,v) \right) dudv \\ &= \frac{1}{2\pi\sqrt{1-\xi^2}} \int_{-\infty}^{\infty} \sin(\Omega_j v + \Phi_j) I_1 dv;\end{aligned}\quad (29)$$

where

$$\begin{aligned}I_1 &= \int_{-\infty}^{\infty} \sin(\Omega_i u + \Phi_i) e^{\frac{-(u^2 - 2\xi uv + v^2)}{2(1-\xi^2)}} du = e^{\frac{-v^2}{2(1-\xi^2)}} \int_{-\infty}^{\infty} \sin(\Omega_i u + \Phi_i) e^{\frac{-(u^2 - 2\xi uv)}{2(1-\xi^2)}} du \\ &= e^{\frac{-v^2 + \xi^2 v^2}{2(1-\xi^2)}} \int_{-\infty}^{\infty} \sin(\Omega_i u + \Phi_i) e^{\frac{-(u^2 - 2\xi uv + \xi^2 v^2)}{2(1-\xi^2)}} du \\ &= e^{-v^2/2} \int_{-\infty}^{\infty} \sin(\Omega_i u + \Phi_i) e^{\frac{-(u-\xi v)^2}{2(1-\xi^2)}} du\end{aligned}\quad (30)$$

By assuming $\eta = u - \xi v$ we will have:

$$I_1 = e^{-v^2/2} \int_{-\infty}^{\infty} \sin(\Omega_i(\eta + \xi v) + \Phi_i) e^{\frac{-\eta^2}{2(1-\xi^2)}} d\eta \quad (31)$$

Before going further, we need to consider the following lemma.

Lemma A.3.

$$\int_{-\infty}^{\infty} \cos(\alpha u + \beta) e^{-\gamma u^2} du = \sqrt{\frac{\pi}{\gamma}} e^{-\frac{\alpha^2}{4\gamma}} \cos \beta, \quad (32)$$

$$\int_{-\infty}^{\infty} \sin(\alpha u + \beta) e^{-\gamma u^2} du = \sqrt{\frac{\pi}{\gamma}} e^{-\frac{\alpha^2}{4\gamma}} \sin \beta \quad (33)$$

The proof is provided in (A.2).

Let $\alpha = \Omega_i$, $\beta = \Omega_i \xi v + \Phi_i$, and $\gamma = \frac{1}{2(1-\xi^2)}$. As a result of equation (33), we have

$$\begin{aligned} I_1 &= e^{-v^2/2} \sqrt{2\pi(1-\xi^2)} e^{\frac{-\Omega_i^2}{2(1-\xi^2)}} \sin(\Omega_i \xi v + \Phi_i) \\ &= \sqrt{2\pi(1-\xi^2)} e^{\frac{-(v^2 + \Omega_i^2(1-\xi^2))}{2}} \sin(\Omega_i \xi v + \Phi_i) \end{aligned} \quad (34)$$

Therefore, based on (29), we will have

$$\begin{aligned} \Delta_{i,j} &= \frac{1}{2\pi\sqrt{1-\xi^2}} \int_{-\infty}^{\infty} \left[\sin(\Omega_j v + \Phi_j) \sqrt{2\pi(1-\xi^2)} e^{\frac{-(v^2 + \Omega_j^2(1-\xi^2))}{2}} \sin(\Omega_i \xi v + \Phi_i) \right] dv \\ &= \frac{e^{\frac{-\Omega_i^2(1-\xi^2)}{2}}}{\sqrt{2\pi}} \int_{-\infty}^{\infty} \left[\sin(\Omega_j v + \Phi_j) e^{-v^2/2} \sin(\Omega_i \xi v + \Phi_i) \right] dv \\ &= \frac{e^{-\Omega_i^2(1-\xi^2)/2}}{\sqrt{2\pi}} \int_{-\infty}^{\infty} e^{-v^2/2} \aleph dv \end{aligned} \quad (35)$$

where

$$\aleph = \frac{1}{2} \left[\cos(v(\Omega_i \xi - \Omega_j) + \Phi_i - \Phi_j) - \cos(v(\Omega_i \xi + \Omega_j) + \Phi_i + \Phi_j) \right] \quad (36)$$

Therefore,

$$\begin{aligned} \Delta_{i,j} &= \frac{e^{-\Omega_i^2(1-\xi^2)/2}}{2\sqrt{2\pi}} \left(\sqrt{2\pi} e^{-(\Omega_i \xi - \Omega_j)^2/2} \cos(\Phi_i - \Phi_j) + \sqrt{2\pi} e^{-(\Omega_i \xi + \Omega_j)^2/2} \cos(\Phi_i + \Phi_j) \right) \\ &= \frac{e^{-\Omega_i^2(1-\xi^2)/2}}{2} \left(e^{-(\Omega_i \xi - \Omega_j)^2/2} \cos(\Phi_i - \Phi_j) + e^{-(\Omega_i \xi + \Omega_j)^2/2} \cos(\Phi_i + \Phi_j) \right) \\ &= \frac{e^{\frac{-\Omega_i^2(1-\xi^2)}{2}} e^{\frac{-(\Omega_i^2 \xi^2 + \Omega_j^2)}{2}}}{2} \left(e^{\Omega_i \Omega_j \xi} \cos(\Phi_i - \Phi_j) + e^{-\Omega_i \Omega_j \xi} \cos(\Phi_i + \Phi_j) \right) \\ &= \frac{e^{\frac{-1}{2}(\Omega_i^2 + \Omega_j^2)}}{2} \left(e^{\Omega_i \Omega_j \xi} \cos(\Phi_i - \Phi_j) + e^{-\Omega_i \Omega_j \xi} \cos(\Phi_i + \Phi_j) \right) \end{aligned} \quad (37)$$

As a result of Equations (25) and (37), we have

$$\begin{aligned} \check{\rho}^*(\xi) &= \sum_{i=1}^{\tau} \sum_{j=1}^{\tau} C_i C_j \Delta_{i,j} \\ &= \frac{1}{2} \sum_{i=1}^{\tau} \sum_{j=1}^{\tau} C_i C_j e^{\frac{-1}{2}(\Omega_i^2 + \Omega_j^2)} \left(e^{\Omega_i \Omega_j \xi} \cos(\Phi_i - \Phi_j) + e^{-\Omega_i \Omega_j \xi} \cos(\Phi_i + \Phi_j) \right) \end{aligned} \quad (38)$$

□

A.2. Proof of Lemma (A.3)

Proof. We want to calculate these integrals:

$$\begin{aligned} I_1 &= \int_{-\infty}^{\infty} \cos(\alpha u + \beta) e^{-\gamma u^2} du, \\ I_2 &= \int_{-\infty}^{\infty} \sin(\alpha u + \beta) e^{-\gamma u^2} du \end{aligned} \quad (39)$$

By adding them we will have

$$\begin{aligned} I_1 + iI_2 &= \int_{-\infty}^{\infty} e^{-\gamma u^2} (\cos(\alpha u + \beta) + i \sin(\alpha u + \beta)) du = \int_{-\infty}^{\infty} e^{i(\alpha u + \beta)} e^{-\gamma u^2} du \\ &= e^{i\beta} \int_{-\infty}^{\infty} e^{-\gamma(u^2 + \frac{\alpha i}{\gamma} u)} du = e^{i\beta} \int_{-\infty}^{\infty} e^{-\gamma(u^2 + \frac{\alpha i}{\gamma} u - \frac{\alpha^2}{4\gamma^2})} e^{-\frac{\alpha^2}{4\gamma}} du \\ &= e^{-\frac{\alpha^2}{4\gamma} + i\beta} \int_{-\infty}^{\infty} e^{-\gamma(u^2 + \frac{\alpha i}{\gamma} u - \frac{\alpha^2}{4\gamma^2})} du = e^{-\frac{\alpha^2}{4\gamma} + i\beta} \underbrace{\int_{-\infty}^{\infty} e^{-\gamma(u + \frac{\alpha i}{2\gamma})^2} du}_{I_3} \end{aligned} \quad (40)$$

where i is the unit imaginary number. Since we know that the integral of an arbitrary Gaussian function is

$$\int_{-\infty}^{\infty} e^{-a(x+b)^2} dx = \sqrt{\frac{\pi}{a}}, \quad (41)$$

we will have $I_3 = \sqrt{\frac{\pi}{\gamma}}$. Therefore,

$$I_1 + iI_2 = \sqrt{\frac{\pi}{\gamma}} e^{-\frac{\alpha^2}{4\gamma} + i\beta} = \sqrt{\frac{\pi}{\gamma}} e^{-\frac{\alpha^2}{4\gamma}} (\cos \beta + i \sin \beta) \quad (42)$$

As a result,

$$I_1 = \sqrt{\frac{\pi}{\gamma}} e^{-\frac{\alpha^2}{4\gamma}} \cos \beta, \quad I_2 = \sqrt{\frac{\pi}{\gamma}} e^{-\frac{\alpha^2}{4\gamma}} \sin \beta. \quad (43)$$

□

B. Ablation Studies

In this section, we present ablation studies to demonstrate the effectiveness of STAF.

B.1. Impact of Amplitude, Frequency, and Phase

Figure 12(a) illustrates the PSNR (dB) over 500 iterations for different component combinations: **amplitude** (C_i 's), **frequency** (Ω_i 's), **phase** (Φ_i 's), and their interactions. The model leveraging all three components (freq + phase + amp) achieves the highest PSNR, significantly outperforming individual and partial combinations. This confirms the importance of integrating amplitude, frequency, and phase in the model design for optimal performance, and validates our initial design choices and mathematical analysis.

Additionally, this graph highlights the varying importance of the parameters in our model. Specifically, the amplitudes exhibit the highest significance, followed by the frequencies, with the phases contributing the least. These findings provide valuable guidance for parameter reduction in scenarios with limited training time or hardware resources, enabling more efficient model optimization.

B.2. Comparative Analysis of Activation Strategies

Figure 12(b) aligns with the described strategies in Section 3.4 for implementing STAF's parametric activation functions. The per-neuron activation (green curve) achieves the highest PSNR, demonstrating superior expressiveness, but at the cost

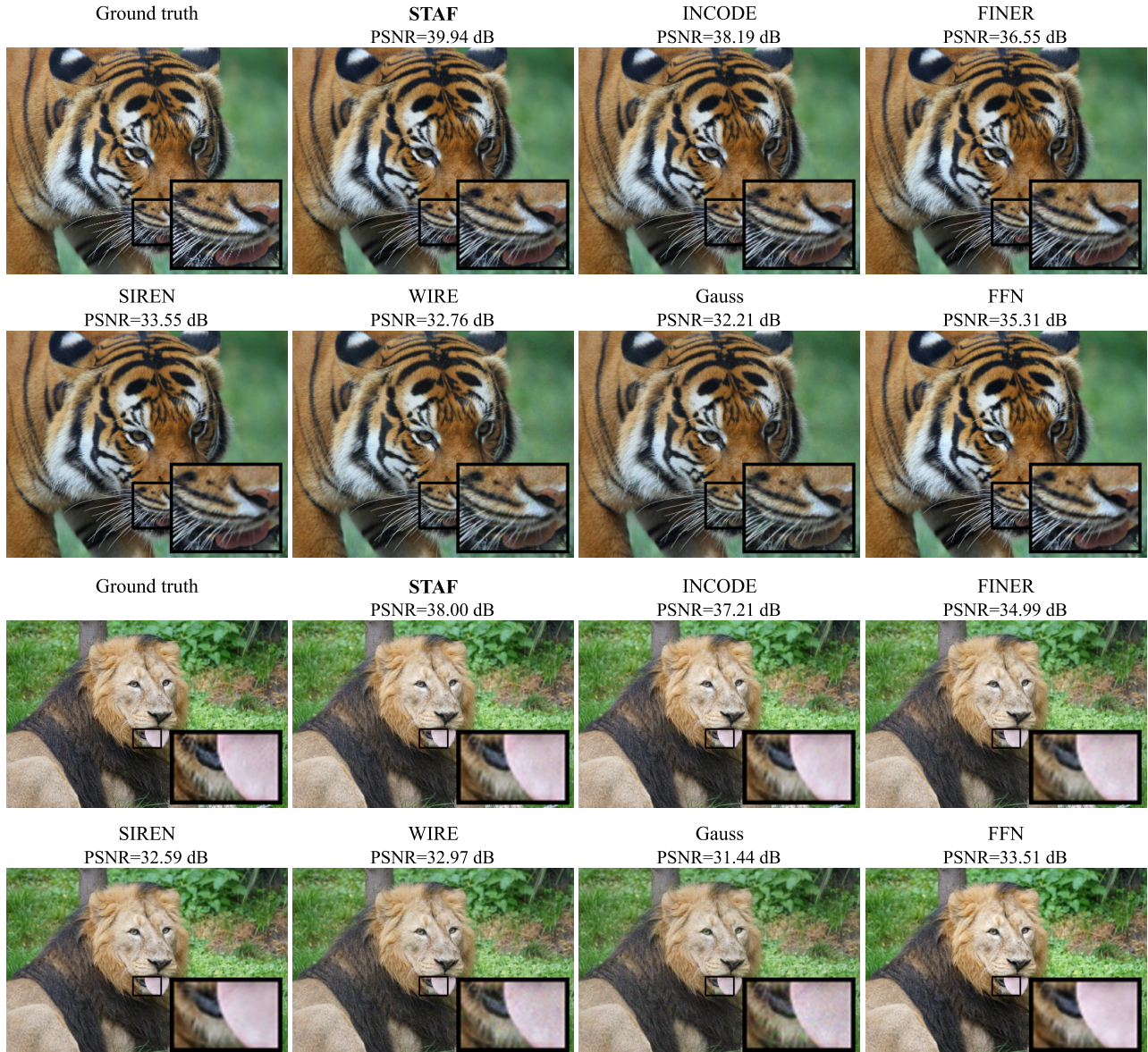


Figure 7. Comparative visualization of image representation with STAF and other activation functions.

of a significant parameter increase, as expected. The network-wide activation (blue curve) shows the weakest performance, reflecting limited expressiveness due to shared activation functions across the entire network. The layer-wise activation (orange curve) offers a balanced trade-off, achieving nearly the same performance as per-neuron activation while requiring far fewer additional parameters (e.g., 225 parameters for a 3-layer MLP with 25 terms). This supports its use as an efficient and effective strategy, as highlighted in Section 3.4.

B.3. Performance Comparison of STAF and SIREN with Similar Parameter Counts

Figure 13 demonstrates the superior performance of STAF compared to SIREN in terms of PSNR (dB) across 250 epochs, despite SIREN having a higher parameter count. To ensure a balanced evaluation, the default configuration of SIREN was modified by adding one additional layer, resulting in 264,193 parameters for SIREN compared to STAF’s 213,761 parameters. This approach avoids extensive parameter tuning for SIREN, offering a practical comparison between the two models. The results clearly show that STAF consistently outperforms SIREN, achieving significantly higher PSNR values

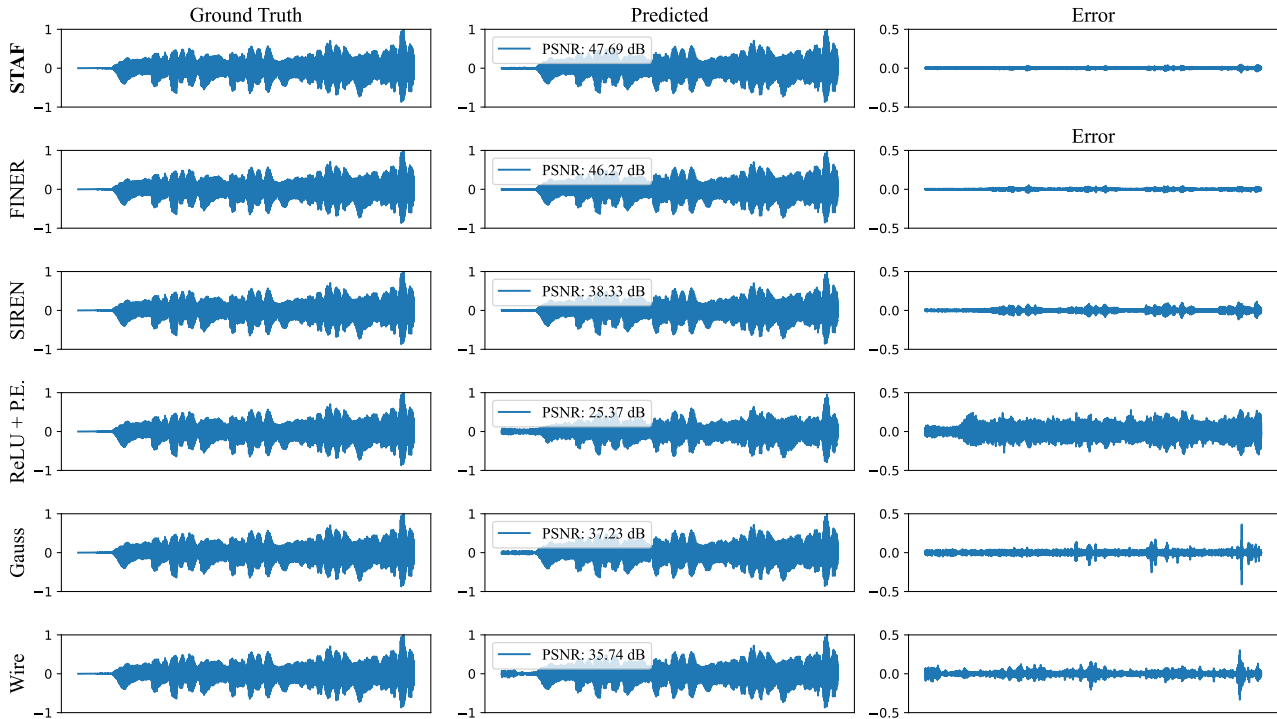


Figure 8. Comparative visualization of audio representation with STAF and other activation functions.

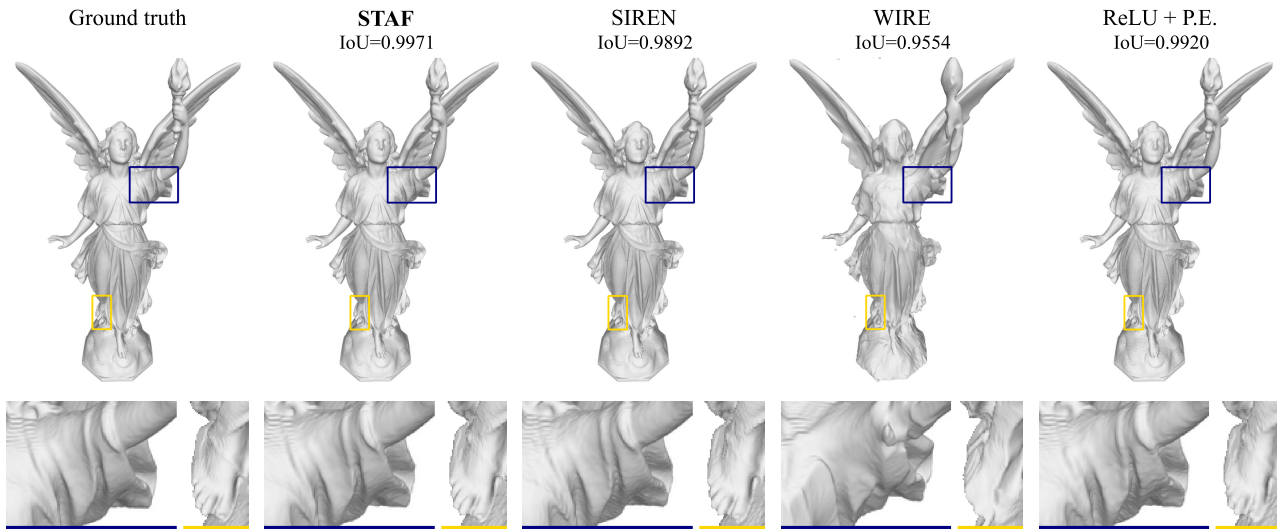


Figure 9. Comparative visualization of shape representation with STAF and other activation functions.

throughout the training process. This highlights STAF’s efficiency and effectiveness, even when constrained to a lower parameter count, making it a more suitable choice for tasks requiring high-quality image reconstruction.

B.4. More Comparative Evaluation

Figure 14 presents a comparative analysis of three methods—STAF, SIREN, and Hash Encoding (Müller et al., 2022)—on the task of high-resolution image reconstruction. The PSNR (dB) curves indicate that STAF significantly outperforms both

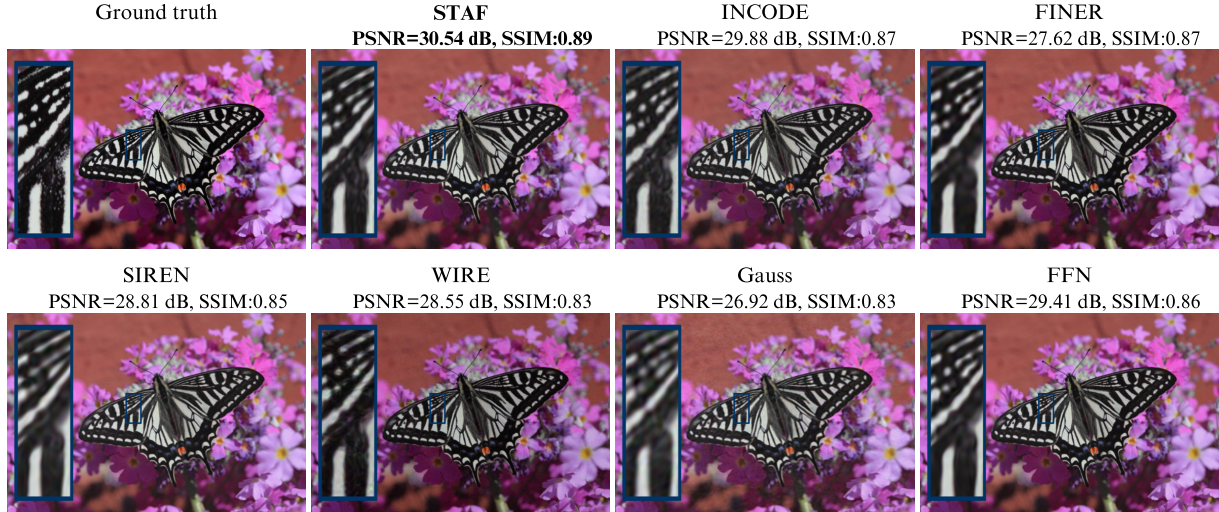


Figure 10. Comparative visualization of 4x super resolution with **STAF** and other activation functions.

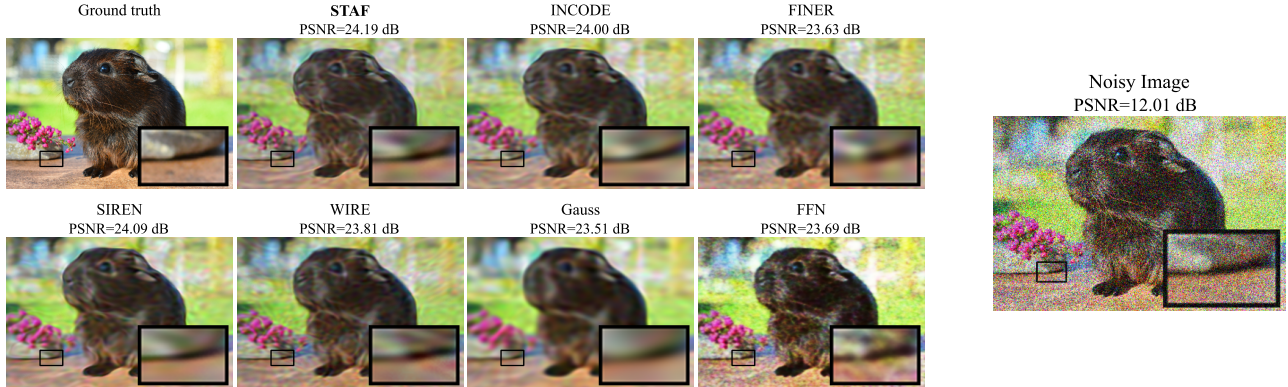


Figure 11. Comparative visualization of image denoising with **STAF** and other activation functions.

SIREN and Hash Encoding, reaching a PSNR of over 100 dB after 500 epochs. While Hash Encoding shows a notable improvement over SIREN, peaking at around 70 dB, it still falls short of STAF’s superior performance. SIREN, in contrast, exhibits the slowest PSNR growth, achieving only around 38 dB. The qualitative comparisons on the right further support these quantitative results, with STAF closely approximating the ground truth, while Hash Encoding and SIREN produce visibly lower-quality reconstructions. This analysis highlights the advantage of STAF in achieving both higher fidelity and faster convergence in image reconstruction tasks.

C. Proofs

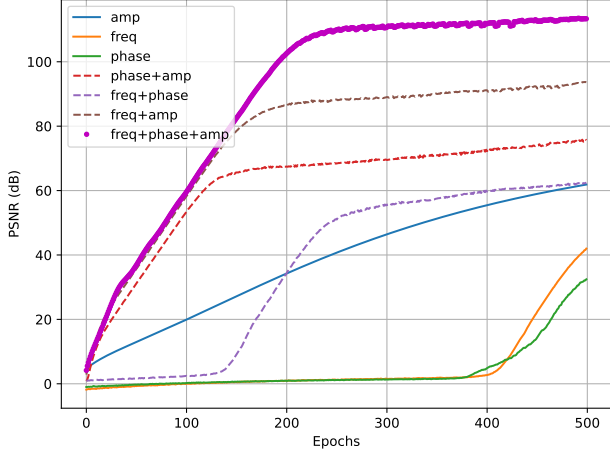
C.1. Proof of Theorem (3.1)

In this section, we provide a step-by-step proof of Theorem (3.1) concerning the initialization scheme of an architecture that leverages STAF.

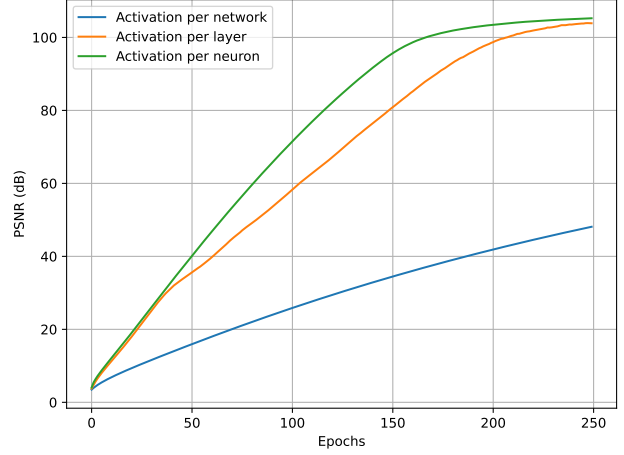
Theorem C.1. Consider the following function Z

$$Z = \sum_{u=1}^{\tau} C_u \sin(\Omega_u \mathbf{w} \cdot \mathbf{x} + \Phi_u) \quad (44)$$

Suppose C_u ’s are symmetric distributions, have finite moments, and are independent of $\Omega_u, \mathbf{w}, \mathbf{x}, \Phi_u$. Furthermore, for



(a) Ablation study of amplitude, frequency, and phase contributions on PSNR performance.



(b) Analysis of activation patterns per network, layer, and neuron on PSNR performance.

Figure 12. (a) Ablation study of amplitude, frequency, and phase contributions on PSNR performance. (b) Analysis of activation patterns per network, layer, and neuron on PSNR performance.

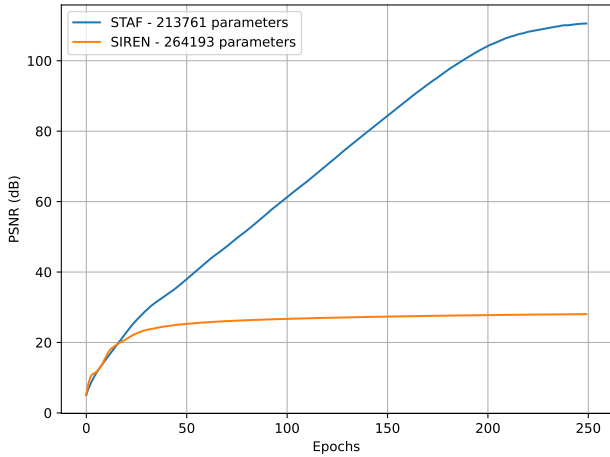


Figure 13. Comparison of PSNR performance between STAF and SIREN over 250 epochs. STAF, with 213,761 parameters, achieves significantly higher PSNR values compared to SIREN, which has 264,193 parameters.

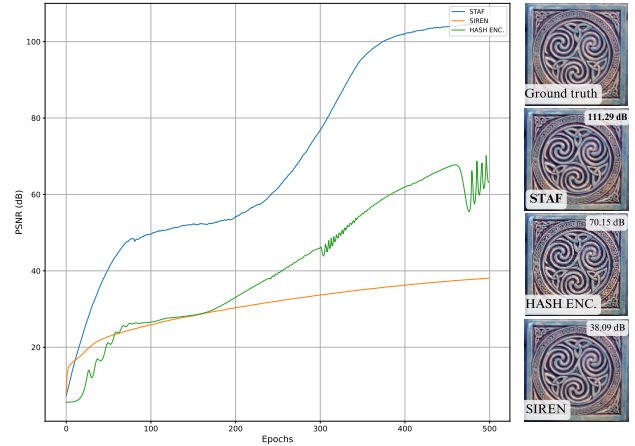


Figure 14. Performance comparison of STAF, SIREN, and Hash Encoding on single image reconstruction. The PSNR curves show that STAF achieves the highest PSNR, followed by Hash Encoding and SIREN.

each u , $\Phi_u \sim U(-\pi, \pi)$. Then the moments of Z will only depend on τ and the moments of C_u 's. Moreover, the odd-order moments of Z will be zero.

Proof. For convenience, let us consider $\Gamma_u = \Omega_u \mathbf{w} \cdot \mathbf{x}$. Based on the multinomial theorem, for every natural number q , we have:

$$Z^q = \sum_{\substack{i_1 + \dots + i_\tau = q \\ i_1, \dots, i_\tau \geq 0}} \left[\binom{q}{i_1, \dots, i_\tau} \prod_{u=1}^{\tau} (C_u \sin(\Gamma_u + \Phi_u))^{i_u} \right].$$

According to the linearity of expected value:

$$\begin{aligned}\mathbb{E}[Z^q] &= \sum_{\substack{i_1+\dots+i_\tau=q \\ i_1, \dots, i_\tau \geq 0}} \left[\binom{q}{i_1, \dots, i_\tau} \mathbb{E} \left[\prod_{u=1}^{\tau} (C_u \sin(\Gamma_u + \Phi_u))^{i_u} \right] \right] \\ &= \sum_{\substack{i_1+\dots+i_\tau=q \\ i_1, \dots, i_\tau \geq 0}} \left[\binom{q}{i_1, \dots, i_\tau} \prod_{u=1}^{\tau} [\mathbb{E}[C_u^{i_u}] \mathbb{E}[\sin^{i_u}(\Gamma_u + \Phi_u)]] \right].\end{aligned}\quad (45)$$

Each choice of i_1, \dots, i_τ is called a partition for q . If q is an odd number, then in each partition of q , at least one of the variables, such as i_k , is odd. Since the function C_i is symmetric, it follows that $\mathbb{E}[C_k^{i_k}] = 0$. This is because odd-order moments of a symmetric distribution are always zero. Consequently, the expectation $\mathbb{E} \left[\prod_{u=1}^{\tau} (C_u \sin(\Gamma_u + \Phi_u))^{i_u} \right]$ also equals zero, as does $\mathbb{E}[Z^q]$.

Now, let us consider the case when q is even. For each partition of q , if at least one of its variables is odd, then, as before, we have $\mathbb{E} \left[\prod_{u=1}^{\tau} (C_u \sin(\Gamma_u + \Phi_u))^{i_u} \right] = 0$. Thus, we can express q as $q = 2j_1 + \dots + 2j_\tau$ where each j_k is a non-negative integer. According to (45), to obtain the i_k -th moment of Z , we need to calculate $\mathbb{E}[\sin^{i_u}(\Gamma_u + \Phi_u)]$. In this case, where $i_u = 2j_u$, $\sin^{i_u} \theta$ is an even function, and its Fourier series consists of a constant term and some cosine terms, given by

$$\sin^{2j_u} \theta = \alpha_0 + \sum_{r=1}^{\infty} \alpha_r \cos(r\theta). \quad (46)$$

Hence,

$$\begin{aligned}\mathbb{E}[\sin^{2j_u}(\Gamma_u + \Phi_u)] &= \mathbb{E}[\alpha_0 + \sum_{r=1}^{\infty} \alpha_r \cos(r(\Gamma_u + \Phi_u))] = \alpha_0 + \sum_{r=1}^{\infty} \alpha_r \mathbb{E}[\cos(r\Gamma_u + r\Phi_u)] \\ &= \alpha_0 + \sum_{r=1}^{\infty} \alpha_r \mathbb{E}[\cos(r\Gamma_u) \cos(r\Phi_u) - \sin(r\Gamma_u) \sin(r\Phi_u)] = \alpha_0 + \sum_{r=1}^{\infty} \alpha_r \Xi\end{aligned}\quad (47)$$

where

$$\Xi = \mathbb{E}[\cos(r\Gamma_u)]\mathbb{E}[\cos(r\Phi_u)] - \mathbb{E}[\sin(r\Gamma_u)]\mathbb{E}[\sin(r\Phi_u)]. \quad (48)$$

Since r is an integer, $r\Phi_u$ will be a period, resulting in $\mathbb{E}[\cos(r\Phi_u)] = \mathbb{E}[\sin(r\Phi_u)] = 0$. Thus, $\mathbb{E}[\sin^{2j_u}(\Gamma_u + \Phi_u)] = \alpha_0$.

Using the formula for the coefficients of the Fourier series, we have:

$$\alpha_0 = \frac{1}{\pi} \int_{-\pi/2}^{\pi/2} \sin^{2j_u} \theta d\theta = \frac{2}{\pi} \int_0^{\pi/2} \sin^{2j_u} \theta d\theta = \frac{2}{\pi} \times \frac{\binom{2j_u}{j_u}}{2^{2j_u}} \times \frac{\pi}{2} = \frac{\binom{2j_u}{j_u}}{2^{2j_u}} \quad (49)$$

where (49) is evaluated using the Wallis integral.

To summarize,

$$\begin{aligned}\mathbb{E}[Z^q] &= \sum_{\substack{j_1+\dots+j_\tau=\frac{q}{2}, \\ j_1, \dots, j_\tau \geq 0}} \binom{q}{2j_1, \dots, 2j_\tau} \prod_{u=1}^{\tau} \mathbb{E}[C_u^{2j_u}] \frac{\binom{2j_u}{j_u}}{2^{2j_u}} \\ &= \sum_{\substack{j_1+\dots+j_\tau=\frac{q}{2}, \\ j_1, \dots, j_\tau \geq 0}} \left[\left(\binom{q}{2j_1, \dots, 2j_\tau} \prod_{u=1}^{\tau} \binom{2j_u}{j_u} \right) \prod_{u=1}^{\tau} \frac{1}{2^{2j_u}} \prod_{u=1}^{\tau} \mathbb{E}[C_u^{2j_u}] \right]\end{aligned}\quad (50)$$

This also accounts for odd-order moments, as it is impossible to select a combination of non-negative integers that sums to a non-integer value.

It is worth noting that:

$$\begin{aligned} \binom{q}{2j_1, \dots, 2j_\tau} \prod_{u=1}^{\tau} \binom{2j_u}{j_u} &= \frac{q!}{(2j_1)! \dots (2j_\tau)!} \times \frac{(2j_1)!}{(j_1)!^2} \times \dots \times \frac{(2j_\tau)!}{(j_\tau)!^2} = \frac{q!}{(j_1!)^2 \dots (j_\tau!)^2} \\ &= \binom{q}{j_1, j_1, \dots, j_\tau, j_\tau} \end{aligned} \quad (51)$$

Furthermore,

$$\prod_{u=1}^{\tau} \frac{1}{2^{2j_u}} = \frac{1}{2^{2 \sum_{u=1}^{\tau} j_u}} = \frac{1}{2^q} \quad (52)$$

By utilizing Equations (50) to (52), we can conclude that:

$$\mathbb{E}[Z^q] = \frac{1}{2^q} \sum_{\substack{j_1 + \dots + j_\tau = \frac{q}{2} \\ j_1, \dots, j_\tau \geq 0}} \binom{q}{j_1, j_1, \dots, j_\tau, j_\tau} \prod_{u=1}^{\tau} \mathbb{E}[C_u^{2j_u}] \quad (53)$$

As you can see, the moments of Z depend solely on τ and the moments of the C_u 's. \square

Now, our goal is to determine the distribution of the C_u 's so that the distribution of Z becomes $\mathcal{N}(0, 1)$. To achieve this, let's first consider the following theorem:

Theorem C.2. (Page 353 of (Shiryaev, 2016)) *Let $X \sim \mathcal{N}(0, \sigma^2)$. Then*

$$E(X^q) = \begin{cases} 0, & \text{if } q \text{ is odd} \\ \frac{q!}{2^{q/2}} \sigma^q, & \text{if } q \text{ is even} \end{cases} \quad (54)$$

and these moments pertain exclusively to the normal distribution.

In theorem (C.1), we proved that for odd values of q , $\mathbb{E}[h^q] = 0$. Thus, in order to have $Z \sim \mathcal{N}(0, 1)$, for even values of q , we must have $\mathbb{E}[h^q] = \frac{q!}{2^{q/2}}$. Alternatively, we can express it as

$$\frac{1}{2^q} \sum_{\substack{j_1 + \dots + j_\tau = \frac{q}{2} \\ j_1, \dots, j_\tau \geq 0}} \binom{q}{j_1, j_1, \dots, j_\tau, j_\tau} \prod_{u=1}^{\tau} \mathbb{E}[C_u^{2j_u}] = \frac{q!}{2^{q/2}}. \quad (55)$$

Simplifying further, we obtain

$$\frac{q!}{2^q} \sum_{\substack{j_1 + \dots + j_\tau = \frac{q}{2} \\ j_1, \dots, j_\tau \geq 0}} \frac{\prod_{u=1}^{\tau} \mathbb{E}[C_u^{2j_u}]}{(j_1!)^2 \dots (j_\tau!)^2} = \frac{q!}{2^{q/2}}. \quad (56)$$

This equation can be further simplified to

$$\sum_{\substack{j_1 + \dots + j_\tau = \frac{q}{2} \\ j_1, \dots, j_\tau \geq 0}} \frac{\prod_{u=1}^{\tau} \mathbb{E}[C_u^{2j_u}]}{(j_1!)^2 \dots (j_\tau!)^2} = \frac{2^{q/2}}{q!}. \quad (57)$$

Equation (57) provides a general formula that can be utilized in further research. It allows for finding different solutions for C_u under various assumptions (e.g., independence or specific dependencies) and different values of τ . However, in the subsequent analysis, we assume that C_u 's are independent and identically distributed (i.i.d) random variables. The following theorem aims to satisfy Equation (57).

Theorem C.3. *Suppose C_u 's are i.i.d random variables with the following even-order moments:*

$$\mathbb{E}[C_u^{2j}] = \left(\frac{2}{\tau}\right)^j j! \quad (58)$$

Then, for every non-negative even number q , Equation (57) holds.²

²If you wonder how this solution struck our mind, you can start by solving equation (57) for $q = 2$ to obtain $\mathbb{E}[h^2]$. Then, using the value of $\mathbb{E}[h^2]$, solve (57) for $q = 4$ to obtain $\mathbb{E}[h^4]$, and so on.

Proof. We begin by simplifying the expression:

$$\begin{aligned}
 & \sum_{\substack{j_1+\dots+j_\tau=\frac{q}{2} \\ j_1, \dots, j_\tau \geq 0}} \frac{\prod_{u=1}^{\tau} \mathbb{E}[C_u^{2j_u}]}{(j_1!)^2 \dots (j_\tau!)^2} = \sum_{\substack{j_1+\dots+j_\tau=\frac{q}{2} \\ j_1, \dots, j_\tau \geq 0}} \frac{\prod_{u=1}^{\tau} \left[\left(\frac{2}{\tau} \right)^j j! \right]}{(j_1!)^2 \dots (j_\tau!)^2} \\
 &= \sum_{\substack{j_1+\dots+j_\tau=\frac{q}{2} \\ j_1, \dots, j_\tau \geq 0}} \left(\frac{2}{\tau} \right)^{\sum_{u=1}^{\tau} j_u} \left(\frac{1}{j_1! \dots j_\tau!} \right) = \sum_{\substack{j_1+\dots+j_\tau=\frac{q}{2} \\ j_1, \dots, j_\tau \geq 0}} \left(\frac{2}{\tau} \right)^{\frac{q}{2}} \left(\frac{1}{j_1! \dots j_\tau!} \right) \\
 &= \left(\frac{2}{\tau} \right)^{\frac{q}{2}} \sum_{\substack{j_1+\dots+j_\tau=\frac{q}{2} \\ j_1, \dots, j_\tau \geq 0}} \frac{1}{j_1! \dots j_\tau!} = \left(\frac{2}{\tau} \right)^{\frac{q}{2}} \frac{1}{\left(\frac{q}{2} \right)!} \sum_{\substack{j_1+\dots+j_\tau=\frac{q}{2} \\ j_1, \dots, j_\tau \geq 0}} \frac{\left(\frac{q}{2} \right)!}{j_1! \dots j_\tau!} \\
 &= \left(\frac{2}{\tau} \right)^{\frac{q}{2}} \frac{1}{\left(\frac{q}{2} \right)!} \sum_{\substack{j_1+\dots+j_\tau=\frac{q}{2} \\ j_1, \dots, j_\tau \geq 0}} \binom{\frac{q}{2}}{j_1, \dots, j_\tau} \tag{59}
 \end{aligned}$$

Based on the multinomial theorem, we can conclude that

$$\left(\frac{2}{\tau} \right)^{\frac{q}{2}} \frac{1}{\left(\frac{q}{2} \right)!} \sum_{\substack{j_1+\dots+j_\tau=\frac{q}{2} \\ j_1, \dots, j_\tau \geq 0}} \binom{\frac{q}{2}}{j_1, \dots, j_\tau} = \left(\frac{2}{\tau} \right)^{\frac{q}{2}} \frac{\tau^{\frac{q}{2}}}{\left(\frac{q}{2} \right)!} = \frac{2^{\frac{q}{2}}}{\left(\frac{q}{2} \right)!} \tag{60}$$

□

Also note that according to Theorem (C.1), the odd-order moments of Z are zero, just like a normal distribution.

Corollary C.4. *Let Z be the random variable defined in (44). Additionally, assume that the C_u 's ($1 \leq u \leq \tau$) used in the definition of Z , are i.i.d random variables with even moments as defined in theorem (C.3). Then $Z \sim \mathcal{N}(0, 1)$.*

Proof. We know that if the MGF of a distribution exists, then the moments of that distribution can uniquely determine its PDF. That is, if X and Y are two distributions and for every natural number k , $E(X^k) = E(Y^k)$, then $X = Y$.

In the Theorem (C.3), we observed that the moments of Z are equal to the moments of a standard normal distribution. Since the MGF of this distribution exists, $Z \sim \mathcal{N}(0, 1)$. □

Now, let's explore which distribution can produce the moments defined in equation (58). To have an inspiration, note that for a centered Laplace random variable X with scale parameter b , we have the PDF of X as

$$f_X(x) = \frac{1}{2b} e^{-\frac{|x|}{b}} \tag{61}$$

and the moments of X given by

$$\mathbb{E}[X^q] = \begin{cases} 0, & \text{if } q \text{ is odd} \\ \frac{b^q}{q!}, & \text{if } q \text{ is even} \end{cases} \tag{62}$$

Hence, the answer might be similar to this distribution. If we assume $Y = \text{sgn}(X)\sqrt{|X|}$, since Y is symmetric, all of its odd-order moments are zero. Now, let us calculate its even-order moments:

$$\mathbb{E}[Y^{2q}] = \mathbb{E}[|X|^q] = \int_{-\infty}^{\infty} |x|^q \frac{1}{2b} e^{-\frac{|x|}{b}} dx = 2 \int_0^{\infty} |x|^q \frac{1}{2b} e^{-\frac{|x|}{b}} dx = \frac{1}{b} \int_0^{\infty} x^q e^{-\frac{x}{b}} dx \tag{63}$$

By assuming $u = \frac{x}{b}$, we will have

$$\mathbb{E}[Y^{2q}] = \int_0^{\infty} (bu)^q e^{-u} du = b^q \int_0^{\infty} u^q e^{-u} du = b^q \Gamma(q+1) = b^q q! \tag{64}$$

By assuming $b = \frac{2}{\tau}$, (58) will be obtained.

The next theorem will obtain the probability distribution function of Y .

Theorem C.5. Let X be a centered Laplace random variable with scale parameter b , and $Y = \text{sgn}(X)\sqrt{|X|}$. Then

$$f_Y(y) = \frac{|y|}{b} e^{-\frac{y^2}{b}} \quad (65)$$

Proof. Let $A = Y^2 = |X|$. Therefore,

$$M_A(t) = \sum_{k=0}^{\infty} \frac{t^k \mathbb{E}[|X|^k]}{k!} \quad (66)$$

As we calculated in (64), $\mathbb{E}[|X|^k] = b^k k!$. Therefore,

$$M_A(t) = \sum_{k=0}^{\infty} \frac{t^k \cdot b^k k!}{k!} = \sum_{k=0}^{\infty} (bt)^k = \frac{1}{1-bt} = \frac{\frac{1}{b}}{\frac{1}{b}-t} \quad (67)$$

that is the MGF of exponential distribution with parameter $\frac{1}{b}$. That is,

$$f_A(a) = \frac{1}{b} e^{-\frac{a}{b}} \quad (68)$$

Therefore, using the fact that A is always non-negative, we consider non-negative values a^2 to describe its cumulative distribution function.

$$F_A(y^2) = \mathbb{P}(A \leq y^2) = 1 - e^{-\frac{y^2}{b}} \quad (69)$$

On the other hand, if $y \geq 0$,

$$\mathbb{P}(A \leq y^2) = \mathbb{P}(Y^2 \leq y^2) = \mathbb{P}(-y \leq Y \leq y) \quad (70)$$

Since we want Y to be symmetric, we assume³

$$\mathbb{P}(-y \leq Y \leq y) = 2 \mathbb{P}(0 \leq Y \leq y) = 2 (\mathbb{P}(Y \leq y) - \frac{1}{2}) = 2F_Y(y) - 1, \quad y \geq 0 \quad (71)$$

Using equations (69) to (71), we draw conclusion that

$$2F_Y(y) - 1 = 1 - e^{-\frac{y^2}{b}}, \quad y \geq 0 \quad (72)$$

By differentiating both sides of (72) with respect to y , we will have

$$2f_Y(y) = \frac{2y}{b} e^{-\frac{y^2}{b}}, \quad y \geq 0 \quad (73)$$

Therefore,

$$f_Y(y) = \frac{y}{b} e^{-\frac{y^2}{b}}, \quad y \geq 0 \quad (74)$$

Since we assumed $y \geq 0$ in the above equations, and we supposed that Y is symmetric,

$$f_Y(y) = \frac{|y|}{b} e^{-\frac{y^2}{b}}, \quad y \in \mathbb{R} \quad (75)$$

Just to make sure that our assumption about the symmetry of Y was correct (or sufficed for our purpose), let us check the even-order moments of Y . The odd-orders are zero based on the symmetry.

$$\mathbb{E}[Y^{2k}] = \int_{-\infty}^{\infty} y^{2k} \left(\frac{|y|}{b} e^{-\frac{y^2}{b}} \right) dy = \frac{2}{b} \int_0^{\infty} y^{2k+1} e^{-\frac{y^2}{b}} dy \quad (76)$$

Setting $y^2 = t$ and $\frac{1}{b} = s$, leads to the following equation:

$$\mathbb{E}[Y^{2k}] = \frac{1}{b} \int_0^{\infty} t^k e^{-st} dt \quad (77)$$

³In fact, the assumption that Y is symmetric is not unexpected, since all odd-order moments of Y are zero. But there are some non-symmetrical distributions whose all odd-order moments are zero (Churchill, 1946). Nevertheless, under some assumptions, it can be shown that a distribution is symmetric if and only if all its odd-order moments are zero. However, we don't use this claim in this paper.

That is the Laplace transform of t^k . Therefore,

$$\mathbb{E}[Y^{2k}] = s \frac{\Gamma(k+1)}{s^{k+1}} = \frac{k!}{s^k} = b^k k! \quad (78)$$

□

In summary, in this section we calculated the initial coefficients of our activation function as described in Theorem (C.5), where we set $b = \frac{2}{\tau}$. Consequently, if we denote the post-activation of layer l by $z^{(l)}$, we will have $z_i^{(l)} \sim \mathcal{N}(0, 1)$ for all $l \in \{2, 3, \dots, L-1\}$, and $i \in \{1, \dots, F_l\}$. This result can be proved by induction on l , using the fact that, based on the theorems in this section, the PDF of Z is independent of the PDF of x .

C.2. Proof of Theorem (5.5)

Before proving the theorem, note the following remark:

Remark C.6. Let X be a $\chi_1 \times \chi_2$ matrix, and Y be a $\gamma_1 \times \gamma_2$ matrix. Then, according to (Ashendorf et al., 2014; Albrecht et al., 2023):

$$(X \otimes Y)_{i,j} = x_{[i/\gamma_1], [i/\gamma_2]} y_{(i-1)\% \gamma_1 + 1, (j-1)\% \gamma_2 + 1}. \quad (79)$$

Now, let us consider each pair of layers as a block, where the first two layers form the first block, the second two layers form the second block, and so on. We prove the theorem by induction on the block numbers. The proof consists of three parts:

Part 1) Consider the weight matrix and bias vector given by:

$$\overline{\mathbf{W}}^{(l)} = \mathbf{\Omega} \otimes \mathbf{W}^{(l)}, \quad \overline{\mathbf{B}}^{(l)} = \mathbf{\Phi} \otimes \mathbf{J}_{F_l, 1}. \quad (80)$$

We then define

$$\left[\overline{a}_1^{(l)} \quad \overline{a}_2^{(l)} \quad \dots \quad \overline{a}_{\tau F_l}^{(l)} \right]^{tr} = \overline{\mathbf{W}}^{(l)} \mathbf{z}^{(l-1)} + \overline{\mathbf{B}}^{(l)}, \quad (81)$$

and

$$\overline{z}_p^{(l)} = \rho(\overline{a}_p^{(l)}) \quad \forall p \in \{1, 2, \dots, \tau F_l\}. \quad (82)$$

Additionally, define

$$\tilde{a}^{(l+1)} = \left(\mathbf{C}^{tr} \otimes \mathbf{W}_{i,:}^{(l+1)} \right) \overline{\mathbf{z}}^{(l)}, \quad (83)$$

where $W_{i,:}^{(l+1)}$ denotes the i 'th row of $W^{(l+1)}$. Then, we can observe that

$$\tilde{a}^{(l+1)} = a_i^{(l+1)} \quad (84)$$

Proof. First, let us calculate $a_i^{(l+1)}$ using activation function ρ^* . Note that $a^{(l+1)} = \mathbf{W}^{(l+1)} \mathbf{z}^{(l)}$. Therefore, $a_i^{(l+1)} = \mathbf{W}^{(l+1)}_{i,:} \mathbf{z}^{(l)}$. It implies that

$$\begin{aligned} a_i^{(l+1)} &= \sum_{j=1}^{F_l} W_{i,j}^{(l+1)} z_j^{(l)} = \sum_{j=1}^{F_l} W_{i,j}^{(l+1)} \rho^*(a_j^{(l)}) = \sum_{j=1}^{F_l} W_{i,j}^{(l+1)} \rho^* \left(\sum_{k=1}^{F_{l-1}} W_{j,k}^{(l)} z_k^{(l-1)} \right) \\ &= \sum_{j=1}^{F_l} W_{i,j}^{(l+1)} \sum_{m=1}^{\tau} \mathbf{C}_m \rho \left(\mathbf{\Omega}_m \sum_{k=1}^{F_{l-1}} W_{j,k}^{(l)} z_k^{(l-1)} + \mathbf{\Phi}_m \right) \end{aligned} \quad (85)$$

Next, let us calculate $\tilde{a}^{(l+1)}$. We have

$$\begin{aligned} \overline{a}_p^{(l)} &= \left[\overline{\mathbf{W}}^{(l)} \mathbf{z}^{(l-1)} + \overline{\mathbf{B}}^{(l)} \right]_p = \overline{\mathbf{W}}^{(l)}_{p,:} \mathbf{z}^{(l-1)} + \overline{\mathbf{B}}^{(l)}_p = \sum_{k=1}^{F_{l-1}} \left(\overline{\mathbf{W}}^{(l)}_{p,k} z_k^{(l-1)} \right) + \overline{\mathbf{B}}^{(l)}_p \\ &= \sum_{k=1}^{F_{l-1}} \left(\mathbf{\Omega}_{[p/F_l], [k/F_{l-1}]} W_{1+(p-1)\%F_l, 1+(k-1)\%F_{l-1}}^{(l)} z_k^{(l-1)} \right) + \mathbf{\Phi}_{[p/F_l]} \end{aligned} \quad (86)$$

Equation (86) is based on equation (79). Since $1 \leq k \leq F_{l-1}$, it follows that $\lceil k/F_{l-1} \rceil = 1$ and $(k-1)\%F_{l-1} = k-1$. As a result,

$$\begin{aligned} \overline{a_p^{(l)}} &= \sum_{k=1}^{F_{l-1}} \left(\Omega_{\lceil p/F_l \rceil} W_{1+(p-1)\%F_l, k}^{(l)} z_k^{(l-1)} \right) + \Phi_{\lceil p/F_l \rceil} \\ &= \Omega_{\lceil p/F_l \rceil} \sum_{k=1}^{F_{l-1}} \left(W_{1+(p-1)\%F_l, k}^{(l)} z_k^{(l-1)} \right) + \Phi_{\lceil p/F_l \rceil} \end{aligned} \quad (87)$$

Therefore,

$$\overline{z_p^{(l)}} = \rho \left(\Omega_{\lceil p/F_l \rceil} \sum_{k=1}^{F_{l-1}} \left(W_{1+(p-1)\%F_l, k}^{(l)} z_k^{(l-1)} \right) + \Phi_{\lceil p/F_l \rceil} \right) \quad (88)$$

Consequently,

$$\begin{aligned} \tilde{a}^{(l+1)} &= \sum_{p=1}^{\tau F_l} \left[\mathbf{C}^{tr} \otimes W_{i,:}^{(l+1)} \right]_{1,p} \overline{z_p^{(l)}} = \sum_{p=1}^{\tau F_l} \mathbf{C}_{1, \lceil p/F_l \rceil}^{tr} W_{i, 1+(p-1)\%F_l}^{(l+1)} \overline{z_p^{(l)}} \\ &= \sum_{p=1}^{\tau F_l} \mathbf{C}_{\lceil p/F_l \rceil} W_{i, 1+(p-1)\%F_l}^{(l+1)} \overline{z_p^{(l)}} \end{aligned} \quad (89)$$

$$= \sum_{j=1}^{F_l} \sum_{m=1}^{\tau} \mathbf{W}_{i,j}^{(l+1)} \overline{\mathbf{C}_{m, z_{F_l(m-1)+j}^{(l)}}} \quad (90)$$

Equation (90) is obtained as follows: by changing the indices of \mathbf{W} and \mathbf{C} from equation (89) to (90), we need to change the index of $z^{(l)}$ too. To this end, note that

$$m = \lceil p/F_l \rceil, \quad j = 1 + (p-1)\%F_l \quad (91)$$

If $F_l \nmid p$, then $m = 1 + \lceil p/F_l \rceil$. As we know, $p = F_l \lceil p/F_l \rceil + p\%F_l$. Therefore, $p = F_l(m-1) + j$. This equation also holds when $F_l \mid p$.

Equation (90) can be rewritten as follows:

$$\sum_{j=1}^{F_l} \mathbf{W}_{i,j}^{(l+1)} \sum_{m=1}^{\tau} \overline{\mathbf{C}_{m, z_{F_l(m-1)+j}^{(l)}}} \quad (92)$$

where, according to equations (88) and (91),

$$\overline{z_{F_l(m-1)+j}^{(l)}} = \rho \left(\Omega_m \sum_{k=1}^{F_{l-1}} \left(W_{j,k}^{(l)} z_k^{(l-1)} \right) + \Phi_m \right) \quad (93)$$

Hence,

$$\tilde{a}^{(l+1)} = \sum_{j=1}^{F_l} \mathbf{W}_{i,j}^{(l+1)} \sum_{m=1}^{\tau} \mathbf{C}_m \rho \left(\Omega_m \sum_{k=1}^{F_{l-1}} \left(W_{j,k}^{(l)} z_k^{(l-1)} \right) + \Phi_m \right) \quad (94)$$

which is equal to $a_i^{(l+1)}$ based on (85). \square

Part 2) Let $\overline{\mathbf{B}^{(l+1)}} = \Phi \otimes \mathbf{J}_{F_{l+1}, 1}$. We can define $\overline{a^{(l+1)}}$ as follows:

$$\left[\overline{a_1^{(l+1)}} \quad \overline{a_2^{(l+1)}} \quad \dots \quad \overline{a_{\tau(F_{l+1})}^{(l+1)}} \right]^{tr} = \Omega \otimes \mathbf{a}^{(l+1)} + \overline{\mathbf{B}^{(l+1)}}. \quad (95)$$

Therefore, using Equations (83), (84) and (95), we can write

$$\overline{a^{(l+1)}} = \overline{W^{(l+1)}} \overline{z^{(l)}} + \overline{B^{(l+1)}} \quad (96)$$

, where

$$\overline{W^{(l+1)}} = \Omega \otimes \left(C^{tr} \otimes W^{(l+1)} \right) = (\Omega \otimes C^{tr}) \otimes W^{(l+1)}. \quad (97)$$

Moreover, if we define

$$\overline{z_q^{(l+1)}} = \rho \left(\overline{a_q^{(l+1)}} \right) \quad \forall q \in \{1, \dots, \tau(F_{l+1})\}, \quad (98)$$

we can observe that

$$\mathbf{z}^{(l+1)} = (C^{tr} \otimes I_{F_{l+1}}) \overline{\mathbf{z}^{(l+1)}}. \quad (99)$$

Proof. We know that

$$z_i^{(l+1)} = \rho^*(a_i^{(l+1)}) = \sum_{n=1}^{\tau} \rho \left(\Omega_n a_i^{(l+1)} + \Phi_n \right). \quad (100)$$

Now, let us calculate each entry of the RHS of Equation (99)

$$\left[(C^{tr} \otimes I_{F_{l+1}}) \overline{\mathbf{z}^{(l+1)}} \right]_i = \left[C^{tr} \otimes I_{F_{l+1}} \right]_i \overline{\mathbf{z}^{(l+1)}} = \sum_{j=1}^{\tau F_{l+1}} (C^{tr} \otimes I_{F_{l+1}})_{i,j} \overline{z^{(l+1)}}_j. \quad (101)$$

Hence, according to (79), we have

$$\left[(C^{tr} \otimes I_{F_{l+1}}) \overline{\mathbf{z}^{(l+1)}} \right]_i = \sum_{j=1}^{\tau F_{l+1}} C_{[i/F_{l+1}], [j/F_{l+1}]}^{tr} \delta_{1+(i-1)\%F_{l+1}, 1+(j-1)\%F_{l+1}} \overline{z^{(l+1)}}_j, \quad (102)$$

in which δ refers to Kronecker delta. As a result,

$$\left[(C^{tr} \otimes I_{F_{l+1}}) \overline{\mathbf{z}^{(l+1)}} \right]_i = \sum_{j=1}^{\tau F_{l+1}} C_{[j/F_{l+1}], [i/F_{l+1}]} \delta_{1+(i-1)\%F_{l+1}, 1+(j-1)\%F_{l+1}} \overline{z^{(l+1)}}_j \quad (103)$$

Note that $1 \leq i \leq F_{l+1}$. Therefore, $[i/F_{l+1}] = 1$, and $(i-1)\%F_{l+1} = i-1$. Hence,

$$\left[(C^{tr} \otimes I_{F_{l+1}}) \overline{\mathbf{z}^{(l+1)}} \right]_i = \sum_{j=1}^{\tau F_{l+1}} C_{[j/F_{l+1}]} \delta_{i, 1+(j-1)\%F_{l+1}} \overline{z^{(l+1)}}_j. \quad (104)$$

Also note that $\delta_{i, 1+(j-1)\%F_{l+1}}$ is zero, except when $j = kF_{l+1} + i$, in which case $\delta_{i, 1+(j-1)\%F_{l+1}} = 1$. Thus,

$$\begin{aligned} \left[(C^{tr} \otimes I_{F_{l+1}}) \overline{\mathbf{z}^{(l+1)}} \right]_i &= \sum_{k=0}^{\tau-1} C_{[(kF_{l+1}+i)/F_{l+1}]} \overline{z^{(l+1)}}_{kF_{l+1}+i} = \sum_{k=0}^{\tau-1} C_{k+[i/F_{l+1}]} \overline{z^{(l+1)}}_{kF_{l+1}+i} \\ &= \sum_{k=0}^{\tau-1} C_{k+1} \overline{z^{(l+1)}}_{kF_{l+1}+i} = \sum_{n=1}^{\tau} C_n \overline{z^{(l+1)}}_{(n-1)F_{l+1}+i} = \sum_{n=1}^{\tau} C_n \rho \left(\overline{a^{(l+1)}}_{(n-1)F_{l+1}+i} \right). \end{aligned} \quad (105)$$

Note that

$$\begin{aligned} \overline{a^{(l+1)}}_{(n-1)F_{l+1}+i} &= \Omega_{[(n-1)F_{l+1}+i]/F_{l+1}} \mathbf{a}^{(l+1)}_{1+(n-1)F_{l+1}+i-1} + \Phi_{[(n-1)F_{l+1}+i]/F_{l+1}} \\ &= \Omega_{n-1+[i/F_{l+1}]} \mathbf{a}^{(l+1)}_{1+(i-1)\%F_{l+1}} + \Phi_{n-1+[i/F_{l+1}]} \end{aligned} \quad (106)$$

Since $\left[\frac{i}{F_{l+1}} \right] = 1$ and $(i-1)\%F_{l+1} = i-1$, we have

$$\overline{a^{(l+1)}}_{(n-1)F_{l+1}+i} = \Omega_n \mathbf{a}^{(l+1)}_i + \Phi_n \quad (107)$$

Finally, utilizing Equations (105) and (107), we deduce that

$$\left[(\mathbf{C}^{tr} \otimes \mathbf{I}_{F_{l+1}}) \overline{\mathbf{z}}^{(l+1)} \right]_i = \sum_{n=1}^{\tau} C_{n\rho} \left(\Omega_n \mathbf{a}^{(l+1)}_i + \Phi_n \right), \quad (108)$$

which is equal to the RHS of the Equation (99).

Part 3) Using parts 1 and 2 of the proof, we can state the theorem for arbitrary even values of L . By setting $l = 1$ in the previous parts, we obtain

$$\overline{\mathbf{W}}^{(1)} = \Omega \otimes \mathbf{W}^{(1)}, \quad \overline{\mathbf{B}}^{(1)} = \Phi \otimes \mathbf{J}_{F_1,1} \quad (109)$$

and

$$\overline{\mathbf{W}}^{(2)} = (\Omega \otimes \mathbf{C}^{tr}) \otimes \mathbf{W}^{(2)}, \quad \overline{\mathbf{B}}^{(2)} = \Phi \otimes \mathbf{J}_{F_2,1}. \quad (110)$$

Thus,

$$\overline{\mathbf{W}}^{(l)} = \begin{cases} \Omega \otimes \mathbf{W}^{(l)}, & \text{if } l = 1 \\ (\Omega \otimes \mathbf{C}^{tr}) \otimes \mathbf{W}^{(l)}, & \text{if } l = 2 \end{cases}, \quad \overline{\mathbf{B}}^{(l)} = \Phi \otimes \mathbf{J}_{F_l,1}. \quad (111)$$

In addition, by setting $L = 2$, we will have $\overline{f_{\theta}}(\mathbf{r}) = \overline{\mathbf{W}}^{(3)} \overline{\mathbf{z}}^{(2)}$. Note that according to the assumptions of the theorem, $\overline{\mathbf{W}}^{(3)} = \mathbf{C}^{tr} \otimes \mathbf{I}_{F_2}$. As a result, $\overline{f_{\theta}}(\mathbf{r}) = \overline{\mathbf{W}}^{(3)} \overline{\mathbf{z}}^{(2)} = (\mathbf{C}^{tr} \otimes \mathbf{I}_{F_2}) \overline{\mathbf{z}}^{(2)}$, which is equal to $\mathbf{z}^{(2)} = f_{\theta}(\mathbf{r})$, as derived in (99). (99). In conclusion, the theorem holds true for $L = 2$.

Now, suppose that Equation (12) holds for $L = 2k$. Consequently,

$$\mathbf{z}^{(2k)} = (\mathbf{C}^{tr} \otimes \mathbf{I}_{F_{2k}}) \overline{\mathbf{z}}^{(2k)} \quad (112)$$

Now, we aim to analyze the case for $L = 2(k+1)$. For this network with two additional layers, we first need to adjust the weight matrix for layer $l = 2k+1$. The new weight matrix will be

$$\overline{\mathbf{W}}^{(2k+1)} = \left(\Omega \otimes \mathbf{W}^{(2k+1)} \right) (\mathbf{C}^{tr} \otimes \mathbf{I}_{F_{2k}}), \quad (113)$$

and the weights and the biases of the two new layers will be

$$\begin{aligned} \overline{\mathbf{W}}^{(2k+2)} &= (\Omega \otimes \mathbf{C}^{tr}) \otimes \mathbf{W}^{(2k+2)}, & \overline{\mathbf{B}}^{(2k+2)} &= \Phi \otimes \mathbf{J}_{F_{2k+2},1}, \\ \overline{\mathbf{W}}^{(2k+3)} &= \mathbf{C}^{tr} \otimes \mathbf{I}_{F_{2k+2}}, & \overline{\mathbf{B}}^{(2k+3)} &= \Phi \otimes \mathbf{J}_{F_{2k+3},1}. \end{aligned} \quad (114)$$

Now, note that

$$\overline{\mathbf{W}}^{(2k+1)} \overline{\mathbf{z}}^{(2k)} = \left(\Omega \otimes \mathbf{W}^{(2k+1)} \right) (\mathbf{C}^{tr} \otimes \mathbf{I}_{F_{2k}}) \overline{\mathbf{z}}^{(2k)}. \quad (115)$$

Therefore, by setting $l = 2k-1$ in Equation (99), or using Equation (112), we obtain

$$\overline{\mathbf{W}}^{(2k+1)} \overline{\mathbf{z}}^{(2k)} = \left(\Omega \otimes \mathbf{W}^{(2k+1)} \right) \mathbf{z}^{(2k)} \quad (116)$$

This is analogous to feeding $\mathbf{z}^{(2k)}$ into a neural network whose first layer has the weight matrix $\Omega \otimes \mathbf{W}^{(2k+1)}$. Since the additional weight matrices and biases are consistent with Parts 1 and 2 of the proof, we can conclude that

$$\overline{f_{\theta}}(\mathbf{r}) = \mathbf{z}^{(2k+2)} = f_{\theta}(\mathbf{r}). \quad (117)$$

□

C.3. Proof of Lemma (5.8)

Proof. Let $[a_{r,1}, a_{r,2}, \dots, a_{r,T}] \in \mathbb{Q}^T$ be the r 'th row of Ψ^{tr} . Now, define a matrix $\hat{\mathbf{A}}$ which is identical to \mathbf{A} except for its r 'th row. This modified row is constructed as follows:

$$\hat{a}_{r,i} = \frac{\sqrt{p_i}}{10^{-\eta} \lfloor 10^{\eta} \sqrt{p_i} \rfloor} (\psi_{r,i} + \epsilon[\psi_{r,i} = 0]) \quad (118)$$

in which p_i is the i 'th prime number, ϵ is the machine precision, $[\cdot]$ is Iverson bracket, and η is a large enough natural number such that $\frac{\sqrt{p_i}}{10^{-\eta} \lceil 10^\eta \sqrt{p_i} \rceil} \approx 1$ (to avoid significant changes in the matrix). At the same time, we must have $|\frac{\sqrt{p_i}}{10^{-\eta} \lceil 10^\eta \sqrt{p_i} \rceil} - 1| \geq \epsilon$ (to prevent it from becoming a rational number).

Let $\alpha_i := \frac{\hat{a}_{r,i}}{\sqrt{p_i}}$. Then, $\alpha_i \in \mathbb{Q} \setminus \{0\}$. Now assume that there is $S = [s_1, \dots, s_T]^{tr} \in Ker(\hat{\mathbf{A}}) \cap \mathbb{Q}^T$. Consequently,

$$\sum_{i=1}^T \hat{a}_{r,i} s_i = 0 \quad (119)$$

As a result,

$$\sum_{i=1}^T \alpha_i \sqrt{p_i} s_i = 0 \quad (120)$$

Note that $\alpha_i s_i \in \mathbb{Q}$. Furthermore, The square roots of all prime numbers are linearly independent over \mathbb{Q} (Stewart, 2022). As a result, $\alpha_i s_i = 0$ for all i . Since $\alpha_i \neq 0$, we must have $s_i = 0$ for all i , that is, $Ker(\hat{\mathbf{A}}) \cap \mathbb{Q}^T = \mathbf{O}$.⁴ \square

⁴Note that all algebraic numbers are computable. This analysis was founded on the computability and expressibility of the square roots of prime numbers in a machine. However, most of the computable numbers are rounded or truncated when stored in a machine. Nevertheless, it is possible to demonstrate theoretically or through simulation that increasing precision can make the aforementioned analysis always feasible.